



Production, purification, and process optimization of intracellular pigment from novel psychrotolerant *Paenibacillus* sp. BPW19

Bhagyashree Padhan, Kasturi Poddar, Debapriya Sarkar, Angana Sarkar*

Department of Biotechnology and Medical Engineering, National Institute of Technology Rourkela, Odisha, 769008, India

ARTICLE INFO

Article history:

Received 31 May 2020

Received in revised form 16 December 2020

Accepted 10 January 2021

Keywords:

Bacterial pigment

Intracellular

Microstructure

Solvent extraction

Chromatography

ABSTRACT

A pink pigment-producing bacterial strain was isolated from wastewater and identified as *Paenibacillus* sp. BPW19. The motile bacterial strain was Gram-positive, acid fermenting, glucose, sucrose utilizing and rod-shaped with an average cell length of 1.55 μm as studied under the Environmental Scanning Electron Microscope. Even though being psychrotolerant, the cell growth condition of BPW19 was optimized as 25 $^{\circ}\text{C}$ along with pH 8, and 2.25% inoculum concentration considering the operational ease of the production. Sonication assisted solvent extraction produced 5.41% crude pigment which showed zones of exclusion against gram-negative strains *Escherichia coli* DH5 α , *Enterobacter* sp. EtK3, and *Klebsiella* sp. SHC1. Gas Chromatography-Mass Spectrometry analysis of the crude pigment exhibited the dominant presence of major compounds as dotriacontane; 3,7 dimethyl 7 octanal; 1-eicosene and erucic acid. While column chromatography (ethanol:chloroform in 1:4 (v/v) ratio) purified pigment was identified as erucic acid using Nuclear Magnetic Resonance with a net yield of 3.06%.

© 2021 The Authors. Published by Elsevier B.V. This is an open access article under the CC BY-NC-ND license (<http://creativecommons.org/licenses/by-nc-nd/4.0/>).

1. Introduction

Pigments and dyes are one of the most utilized supplements used in a wide range of industries including food and beverage, textile, leather, cosmetics, pharmaceuticals, paper, dye-sensitized solar cells, etc. not only to increase the aesthetic of the product but also to improve the taste, quality, and durability of it [1,2]. The demand of the pigments and dyes will see an annual increment of 5% during 2020–2027 from its current market of approximately 33.20 billion US dollars [3]. The post-industrial revolution era experienced a significant increase in market demands of synthetic pigments for their high productivity, high stability, high intensity, low production cost, and varied applications [2]. However, since these pigments directly impact the health and well-being of individuals as well as the environment, they are scrutinized by researchers. Recent reports suggesting the carcinogenic activity of carmoisine or mutagenic activity, allergy, and hyperactivity associated with Tartrazine, Allura Red, Sunset Yellow, and Brilliant blue have made people apprehensive about the use of synthetic pigments and many governments have imposed ban or restrictions on their uses [4]. Apart from these, pigment and dye effluents from

various industries like textile, leather, and pharmaceuticals accumulate and contaminate the aquatic environments. For example, approximately 10,000 different synthetic textile dyes are found in industrial effluents that get deposited in the different biosphere as micropollutants [5–8]. Most of these contaminants are non-biodegradable or on degradation produce carcinogenic compounds [7,9]. Management of such contaminants incurs high cost and complexity of the process, and inefficient removal [6,10]. To overcome these hurdles, complex treatment strategies involving nanomaterials have gained interest [11,12]. Nanostructures degrade dyes and particulate contaminants in an eco-friendly and cost-effective way by advanced oxidation processes such as photocatalysis, sonolysis, and Fenton reactions [13–16]. Lately, several nanoparticles [17,18], composites [19], nanocrystals [9,20,21], sorbents [22–24] have been developed and synthesized for the treatment of water contaminated by dyes and other pollutants.

Though these advanced wastewater treatment strategies have been developed to reduce the toxicity of these persistent micropollutants in the environment, these processes have their shortcomings like the requirement of large infrastructure, huge investment, skilled labor, and nanotoxicity [25]. The best possible alternative to protect the environment, as well as human health, should be re-establishing the interest towards the natural pigment and dyes. Natural pigments from plants and minerals have been used from ancient times due to their compatibility, the presence of bioactive compounds, and less toxicity to the environment [26,27].

* Corresponding author.

E-mail addresses: bhagyashreepadhan96@gmail.com (B. Padhan), kasturi.p93@gmail.com (K. Poddar), deb.apn@gmail.com (D. Sarkar), sarkara@nitrrkl.ac.in (A. Sarkar).

Recently, researchers have been investigating bacterial pigments as a form of natural pigment which has the potential to meet the existing market demands without inducing toxic effects on the environment [28]. Moreover, pigments extracted from bacteria are more advantageous than other natural sources like plants or minerals as bacteria are easily available and can be cultured in large scale bioreactors, can be engineered and optimized to increase the yield, simple and easy downstream processing, low maintenance and no requirement of large arable lands and labor, unlike plant pigments, for cultivation and processing, utilizes food and agricultural wastes as substrates promoting waste minimization [29]. Since seasonal and geographical variations affect plant growth, it eventually limits the overall pigment production from plant sources. Bacterial pigments on the other hand have no seasonal or geographical limitations. They also contain different biological properties like antioxidants, anti-inflammatory, anti-fungal, and anti-carcinogenic properties which makes them suitable for the food and pharmaceutical industries [30]. Apart from food and pharmaceuticals, bacterial pigments have application in several fields such as pigment pyocyanin from *Pseudomonas aeruginosa* as textile dye [31], phycocyanin from *Nostoc linckia* for the synthesis of silver nanoparticles [32], prodigiosin from *Serratia marcescens* for the synthesis of dye-sensitized solar cells [33], Violacein from *Chromobacterium violaceum* as immunostimulator with potential to be applied in immune therapies [34] and many others as listed in Table 1 [35–42]. The applicability of bacterial pigment in various industries displays its potential to compete commercially with the existing synthetic pigments in the market. Optimization of bacterial growth conditions such as temperature, pH, incubation time, etc. along with appropriate pigment isolation methods can produce huge quantities of pigment to sustain its commercial usage. Since bacterial pigments can also be intracellular, the loss of the pigment during the extraction and purification process results in a relatively lower net yield of the pigment than other extracellular bacterial pigments or other plant pigments. Hence, the selection of an appropriate extraction method is crucial for obtaining intracellular bacterial pigment. There are several methods used for extraction of intracellular pigment which involves organic solvents, solid-phase extraction, homogenization, freeze-thaw method, ultrasonication, inorganic acids, Soxhlet method, and others [80]. Amongst all these methods, the solvent extraction method using organic solvents like ethanol and methanol is the simplest and most cost-effective method. These methods can also be used exclusively or in suitable combinations with other methods keeping in view their availability, simplicity, and production cost for higher yields.

To move towards retaining the importance of natural pigment, in this current study bacterial pigment production was investigated. To the best knowledge, the pigment production ability of any strain from the *Paenibacillus* genus is being reported for the first time. The intracellular pigment production ability of the test strain was evaluated and the chief component of the pigment was also

identified along with some characteristic property of the producing strain.

2. Material and methods

2.1. Isolation and identification of pigment-producing bacteria

Wastewater samples collected from the oxidation ponds of Rourkela, India (22.26 °N, 84.85 °E) were spread on Reasoner's2A (R-2A) (M1687, Himedia, USA) agar plates and incubated at 30 °C for 3 days. The pigment-producing colonies of BPW19 were isolated and pure colonies of the strain was obtained by subsequent rounds of quadrant streaking method on sterile agar plates with 1.5 % (w/v) of agar. The strain was further identified by analyzing its 16S rRNA gene [43]. The genomic DNA of the strain was isolated from the cell culture pellet using a standard enzymatic protocol with some modifications along with a Gram-positive control, *Bacillus subtilis*, and a Gram-negative control, *Escherichia coli*. The cell culture was divided into four batches and was primarily subjected to four different types of cell lysis treatment, respectively. The treatment methods include sonication for 30 min; boiling at 100 °C for 15 min; boiling at 100 °C for 10 min followed by sonication for 20 min; alkali lysis using 1 M NaOH for 10 min and adding 1 M HCl to cease the lysis treatment post the incubation period [44].

The genomic DNA was then extracted from the treated cells following the standard enzyme assisted cell disruption procedure followed by solvent extraction using PCI (Phenol:Chloroform: Isoamyl alcohol) in the ratio 25:24:1 and successive purification using ice-cold ethanol. The 16S rRNA gene was particularly amplified with the help of degenerative universal forward primer 27 F and reverse primer 1492R using hot-start PCR (Veriti 96-Well Thermal Cycler, Applied Biosystems, Thermo Fischer Scientific, Singapore) [45]. The amplification of the gene was initiated primarily by denaturing the DNA at 95 °C for 5 min succeeded by 35 complete cycles of the denaturation, annealing, and elongation. Denaturation of the DNA was conducted at 95 °C for 1 min which followed the annealing of the primers with the DNA strands at 52 °C for 50 s and then elongation of the strands for 1.5 min at 72 °C. The final elongation is terminated with an extension of 10 min. The PCR amplified product was purified using a gel extraction kit (Genetix Biotech Asia Pvt Ltd, New Delhi, India) and Sanger sequencing was performed from Eurofins Genomics India Pvt Ltd, Bangalore, India [46]. The obtained sequence was edited using BioEdit (v7.0.5) software to remove terminal noise response during the sequencing. Further, BLASTN (Basic Local Alignment Search Tool for Nucleotide) was performed on the edited sequence using NCBI (National Centre for Biotechnology Information) database to identify the related strains having homologous or identical sequences. The identified homologous strains were aligned by multiple sequence alignment CLUSTALW using MEGA7 software. From this multiple alignment result, the final phylogenetic tree

Table 1
Isolated pigments from different bacterial species.

No.	Bacterial species	Source	Pigment	Application	Reference
1.	<i>Serratia marcescens</i>	American type culture collection	Prodigiosin	Fabric dye	[35]
2.	<i>Chryseobacterium artocarpi</i>	Orchard soil	Flexirubin		[36]
3.	<i>Streptomyces coelicoflavus</i>	Soil	Red pigment	Anthracyclines analog	[37]
4.	<i>Chryseobacterium</i> sp. and <i>Hymenobacter</i> sp.	Soil	Xanthophylls	Dye-sensitized solar cells	[38]
5.	<i>Brevundimonas</i> sp.	Marine water	Astaxanthin		[39]
6.	<i>Lysobacter oligotrophicus</i>	Freshwater, Antarctic	Melanin	Removal of free radicals and ROS	[40]
7.	<i>Pseudomonas</i> spp.	Dairy product	Phycocerythrobilin		[41]
8.	<i>Xanthomonas</i> sp.	Marine soil	Yellow	Fabric dye	[42]
	<i>Sarcina</i> sp.		Orange		
	<i>Rhodotorula</i> sp.		Pink Red		

was constructed using the bootstrap method by the neighbor-joining algorithm in MEGA7 software. For the construction of the phylogenetic tree, an out-group was considered as *Staphylococcus aureus* df5 (LN929744) [47–49].

2.2. Characterization of isolated strains

2.2.1. Chemical characterization

The molecular setup of the cell wall of the isolated strain was characterized by the Gram staining method using Gram Staining Kit (K001, Himedia, Mumbai, India). The metabolic biochemical characterization of the isolated bacterial strain was performed by the IMViC test which includes four different examinations, viz. Indole production test, Methyl red test, Voges-Proskauer test, and Citrate utilization test using IMViC Identification Kit (207900011, Microxpress, Goa, India). The carbohydrate utilization profile of the isolated bacterial strain was performed using different carbohydrate-containing media provided in the same kit [50]. All the biochemical characterization experiments were validated using two model organisms viz. *B. subtilis* and *E. coli*.

2.2.2. Physical characterization

A motility test was performed by the hanging drop method using a circular concavity slide. In a clean glass slide, a single drop of overnight grown culture was placed by micropipette and covered with a concavity slide using petroleum jelly without disturbing the drop. The slide was flipped carefully and the drop was observed under a total of 1000X resolution in a compound microscope to identify any motion inside the hanging drop [51]. To validate the process, *B. subtilis* was used as a positive control and *Klebsiella pneumonia* as a negative control.

The isolated bacteria were further physically characterized by Environmental Scanning Electron Microscope (ESEM). Sample preparation steps include fixation by 2.5 %–3 % glutaraldehyde in phosphate buffer at room temperature for 1–2 h followed by washing in phosphate buffer for 10 min. Post-fixation was done by using 1 %–2 % osmium tetroxide in phosphate buffer for 1–2 h followed by washing in distilled water for 10 min. Next dehydration at different ethanol concentration of 30 %, 40 %, 50 %, 60 %, 70 %, 80 %, 90 % for 10 min at each concentration and dehydration at 100 % ethanol for twice for 20 min. The specimen was then dried and mounted on carbon tape and the sample was viewed under the Environmental Scanning Electron Microscope (ESEM) (Quanta 600 FEG, FEI, Japan) [52]. Moreover, the effect of temperature on bacterial growth was studied for a declining temperature range of 35 °C to 5 °C to evaluate the psychrotolerant nature of the isolated strain.

2.3. Optimization of pigment production

To optimize the biomass production and cellular growth of the isolated strain BPW19, a two-level, three factorial central composite design (CCD) was obtained using Design-Expert software (Trial version). For the biomass production, the three main contributing factors were taken as the incubation temperature, pH and inoculum percentage which are represented as coded values of A, B, and C, respectively [43,53]. The levels for A, B, and C were considered as 25 °C and 37 °C, 6 and 8, 1.5, and 3.5, respectively. A total of 20 run combinations were proposed by the software to obtain the responses of biomass production. For each run, 150 mL of culture was performed in constant shaking of 140 rpm and incubated for 4 days [54].

Analysis of variance (ANOVA) was used to test the effect of different factors on response variables and interaction between the response and the interaction variables were examined using model equations. Error sum of square (SSE), regression sum of square

(SSR) and corrected sum of squares (SST) was determined using ANOVA analysis. Fisher's F-test checked the statistical significance of the model whereas the coefficient of determination R^2 expressed the polynomial model's fit quality. Based on the effect of three factors, the respective contour plots were obtained for both the levels [55,56].

2.4. Bacterial cell harvesting using lab-scale bioreactor

To obtain biomass for pigment production, the isolated bacterial strain was cultured in a total of 2.5 L of R-2A broth in a stirred tank bioreactor (BIOSTAT B plus, Sartorius Stedim Biotech, Germany) constantly maintaining the optimized culture conditions for 4 days in presence of constant shaking of 140 rpm at 25 °C. After the incubation time, the color of the broth was found to be changed to pink. From the broth, the biomass was harvested using centrifugation (5430R, Eppendorf, Germany) at 7000 rpm at room temperature for 15 min. The pellet of the collected biomass from the 2.5 L culture was dried in open air overnight and weighed [57].

2.5. Pigment extraction, purification and yield analysis

The pigment extraction process was initiated by dissolving the whole of the harvested biomass in 50 mL of 100 % methanol (v/v) assisted by vortexing to confirm a homogenous solution. The pigment appeared to be inside the cell as the centrifuged broth exhibited no extraction of the produced pigment. Hence the pigment was concluded to be intracellular. The dissolved cells of isolated bacterial strains were then lysed by ultrasonication treatment in a bath sonicator (Digital Ultrasonic Cleaner LCMU-2, Labman Scientific Instruments, Chennai, India) for 30 min. After sonication, the solution mixture was centrifuged at 7000 rpm at room temperature for 15 min to obtain a colorless pellet and colored supernatant [26,58]. This methanol solution along with the extracted pigment was then air-dried for 3 days in a dust-free environment. After drying, the extracted crude pigment was weighed.

The purification of the crude pigment was performed by Column Chromatography assisted with Thin Layer Chromatography (TLC). Initially, a homogenous mixture of dried crude pigment and silica were prepared and column chromatography was performed using dissolved Silica Gel G (GRM7480, Himedia, New Delhi, India) in chloroform in 1:4 (w/v) ratio. The fractions were eluted using a solvent mixture of ethanol:chloroform in 1:4 (v/v) ratio [59,60]. Each eluted fractions were examined by TLC analysis in pre-coated TLC plates (TLC Silica Gel 60 F₂₅₄, Merck, India) using the same solvent as the mobile phase for examining the purity of the fractions. For each TLC run, the retention factor (R_f) value was calculated by Eq. (1) [27].

$$R_f = \frac{\text{Distance traversed by the pigment}}{\text{Distance traversed by the solvent}} \quad (1)$$

Elute showing single mobile front having identical R_f value was considered as a single component. Such fractions were cumulated and the solvent was evaporated to obtain the purified dried component. From the obtained data, stoichiometric equations were produced to represent each of the steps and net yield was calculated.

2.6. Antibacterial assay

The antibacterial effect of the crude pigment was studied by inoculating it with different Gram-positive and Gram-negative bacterial strains on Luria Bertani (LB) (M575) (Himedia, India) agar media plates. The Gram-negative test organisms include *Escherichia coli* DH5 α , *Enterobacter* sp. EtK3, *Klebsiella* sp. SHC1,

whereas Gram-positive test strain includes *Bacillus subtilis* MTCC 2616. Young suspension cultures of the test strains were spread over in different sterile LB agar plates. Paper discs of mm diameter impregnated with 5 μ L of the pigment suspended in a solvent were placed on the plates and incubated at 30 °C for 3 days. A parallel plate was maintained by using a similar paper disc impregnated with only methanol as a control for the experimental condition. Proper radial diffusion of the pigment was allowed by keeping the plates upright in an undisturbed condition [27,61].

2.7. GC–MS analysis

For the Gas Chromatography–Mass Spectrometry analysis of the crude pigment, a pinch of dried crude pigment was dissolved in 500 μ L of methanol. The sample was analyzed using Gas Chromatography (7890B, Agilent Technologies, United States) using standard HP-5-MS column (7890B, Agilent Technologies, United States) and the compounds were detected by Mass Spectrometer (5977A, Agilent Technologies, United States). The initial temperature of the gas chromatography was maintained at 50 °C and for 1 min and escalated up to 180 °C at a rate of 20 °C/min and held for 0.5 min. The temperature was increased again at a rate of 20 °C/min up to 280 °C and held for 3 min. A split ratio of 1:50 was maintained with Helium being used as inert carrier gas at a flow rate of 1 mL/min [56,62,63].

2.8. NMR analysis of pigment compound

The characterization of the purified pigment was performed by Nuclear Magnetic Resonance (NMR) Spectroscopy. A pinch of dried purified pigment was dissolved in 500 μ L of deuterated dimethyl sulfoxide (DMSO) (DLM-10-S-10 mL, Cambridge Isotope Laboratories Inc, United States) and the solution was made homogenous [64]. The mixture was then analyzed in 400 ultrashield NMR (Avance III, Bruker, United States) to evaluate the number of protons (^1H) at 500.13 MHz and carbon (^{13}C) at 125.77 MHz frequency [61].

2.9. Statistical analysis

The experiments were performed in triplicates and the obtained results were statistically analyzed in Origin Pro (v11.0) using Analysis of Variance (ANOVA) test. The significant difference was calculated statistically using the Chi-Square test.

2.10. Nucleotide sequence accession number

The obtained sequence has been submitted to the GenBank database of the NCBI with an accession number of MK944323.

3. Results and discussion

3.1. Phylogenetic analysis of bacterial strain

The pink-colored colony was collected from the wastewater spread plates and streaked multiple times to screen out the pure strain. DNA extraction of the bacterial strain using enzymatic cell lysis found no yield of genomic DNA, while both the control microbes showed a significant yield of genomic DNA following the same protocol. This indicated high resistivity of the isolated bacterial cell wall towards cell lysis due to its complex cell wall composition. The DNA extraction was successful only after a more vigorous cell lysis approach like sonication or boiling combined with sonication.

BLASTN analysis of the partial sequence of the 16S rRNA gene of BPW19 confirms the relation of the isolated strain to different species of *Paenibacillaceae* family. The phylogenetic analysis showed that *Paenibacillus taichungensis* BCRC 17757 (EU179327) had the most resemblance with BPW19 (MK944323) (Fig. 1). Other closely related bacterial strains were found to be *P. oceanisediminis* L10 (NR118217), *P. dongdonensis* KUDC0114 (KF425513), *P. paucisoli* 1411 (AB245384), and *P. terrae* AM141 (AF391124). This confirmed the relation of the isolated BPW19 with *Paenibacillaceae* family and established it as a member of the family. *Paenibacillaceae* family is well known as a soil bacteria and associated with the growth of different plants like maize, cucumber, rice, pumpkin, etc.

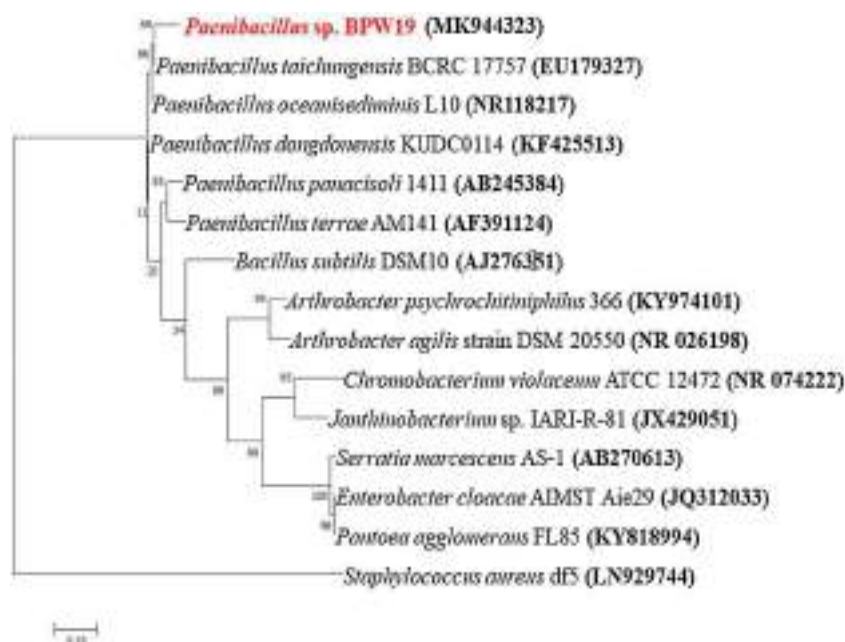


Fig. 1. Phylogenetic tree analysis of the isolated strain BPW19 (MK944323).

showing abilities like nitrogen fixation, phosphate solubilization and iron acquisition [64,65]. Even biocontrol and insecticidal effects along with antimicrobial effects were also observed by members of the *Paenibacillaceae* family [64]. Although no *Paenibacillaceae* family members have been reported in pigment production to date. The phylogenetic analysis also showed that the isolated strain BPW19 is distantly related to *Bacillus subtilis* and other well-known pigment-producing bacteria like *Serratia marcescens*, *Enterobacter cloacae*, *Chromobacterium violaceum*, and *Arthrobacter agilis*. *Staphylococcus aureus* was considered as an outgroup to construct the phylogenetic tree.

3.2. Characterization of strain

The Gram staining differentiates bacterial strains based on their cell wall content: Gram-negative strain containing lower polysaccharide and higher lipid percentage hence staining red by safranin, characterizing less rigid cell wall, and Gram-positive strain having higher polysaccharide and lower lipid content hence staining purple by crystal violet signifying the presence of rigid cell wall. The strain BPW19 was observed to be Gram-positive and rod-shaped characterizing its rigid cell wall which was evident during the cell lysis process of DNA extraction. During the experiment, a Gram-positive control, *B. subtilis*, and a Gram-negative control, *E. coli* was maintained to validate the result.

The ability of the bacterial strain to convert tryptophan into indole was evaluated by the Indole test in which Kovac reagent turns to pinkish-red from colorless in presence of indole. The strain BPW19 did not show any such changes in the color signifying its inability to produce indole from tryptophan. For this analysis, *E. coli* was considered as a positive control, and *B. subtilis* was considered as a negative control. The acid fermentation ability of the isolated strain BPW19 was examined by methyl red test in which the media contained a pH indicator (methyl red) which turns yellow to red in the periphery of a bacterial colony producing acid. BPW19 exhibited similar changes indicating acid fermentation ability. *E. coli* and *B. subtilis* were maintained as a positive and negative control, respectively. The Voges-Proskauer test was used to check the utilization 2,3 butanediol pathway to produce acetoin from glucose by the bacterial strain in which the test reagent containing α -naphthol and potassium hydroxide turns pinkish for a positive result and remain colorless or turns slightly copper for the negative result. The negative results for BPW19 in the Voges-Proskauer test confirmed that the strain cannot produce acetoin by glucose fermentation. *B. subtilis* and *E. coli* were considered as a positive and negative control, respectively for the examination. The citric acid test was conducted to confirm the citrate utilization ability of the bacterial strain as a sole carbon source in which a pH indicator turns blue from green due to the increase in the pH of the media as

citrate gets depleted. No such color changes of the inoculated citrate media were evident in presence of BPW19 which inferred the inability of the strain to utilize citrate as sole carbon source. *B. subtilis* and *E. coli* were considered as positive and negative control, respectively for the analysis. Carbohydrate utilization profile of the isolated strain BPW19 was constructed following the standard protocol. In the process, the carbohydrate utilization activity generally reduces the pH of the medium due to the production of acids like pyruvic acid and other secondary metabolites. This change in the pH was detected by pH indicator phenol red which turns purple-red to yellow in lower pH. Different carbohydrate was considered and it was found that BPW19 was able to utilize glucose and sucrose as sole carbon sources. While the medium containing carbohydrates like adonitol, arabinose, lactose, sorbitol, mannitol, and rhamnose did not show any changes signifying the inability of the strain to utilize these carbohydrates as sole carbon sources. As a reference carbohydrate profile and validation of the experiment, *B. subtilis* and *E. coli* were considered. The comparative biochemical profile of BPW19 had been represented in Table 2 along with the model organisms *B. subtilis* and *E. coli*.

The strain BPW19 appeared motile when observed under 1000X microscopic magnification which states a character for strains of *Paenibacillaceae* family [66]. *B. subtilis* was found motile whereas *K. pneumoniae* was found to be non-motile which ensured the correctness of the experiment. BPW19 appeared rod-shaped with an average cell length of 1.55 μm and was found to have a rough appearance on the cell surface when visualized under 50,000X magnification of the ESEM (Fig. 2). The obtained cell length of BPW19 is smaller than other reported bacterial strains from the *Paenibacillaceae* family, for example, *Paenibacillus dongdonensis*, was reported with an average length of 2.8 μm [67]. On the other hand, BPW19 had larger cell length than bacteria like *S. aureus* which had been reported with an average cell length of 1 μm [68].

3.3. Psychrotolerant nature of BPW19

The bacterial strain was found to grow better in lower temperatures and the cellular growth was observed to be the maximum at 5 °C which is 11.80 % higher than that observed at 25 °C, 60.5 % higher than the growth at 30 °C and almost 296.46 % higher than the growth obtained at 35 °C (Fig. 3). However, the specific growth rate was observed to be more at a higher temperature of 30 °C with 1.64/hr as compared to a lower temperature of 5 °C with 0.66/hr. The cell growth rate at a lower temperature was unsurprisingly lower as the metabolic activities tend to slow down at low temperatures. Since the log phase was more prolonged at lower temperatures, the overall cell growth was obtained higher despite having a lower growth rate. Since BPW19

Table 2
Biochemical characterization of the isolated bacterial strain *Paenibacillus* sp. BPW19.

Biochemical test	Positive	Negative	<i>E. coli</i> (DH5 α)	<i>B. subtilis</i> (MTCC 2616)	BPW19
Gram staining	Violet	Red	–	+	+
Indole test	Reddish pink	Colorless	+	–	–
Methyl red test	Red	Yellowish orange	+	–	+
Voges Prasekeur test	Pinkish red	Colorless	–	+	–
Citrate utilization test	Blue	Green	–	+	–
Glucose	Yellow	Red	+	+	+
Adonitol	Yellow	Red	–	–	–
Arabinose	Yellow	Red	+	+	–
Lactose	Yellow	Red	+	–	–
Sorbitol	Yellow	Red	+	+	–
Mannitol	Yellow	Red	+	+	–
Rhamnose	Yellow	Red	+	–	–
Sucrose	Yellow	Red	–	+	+

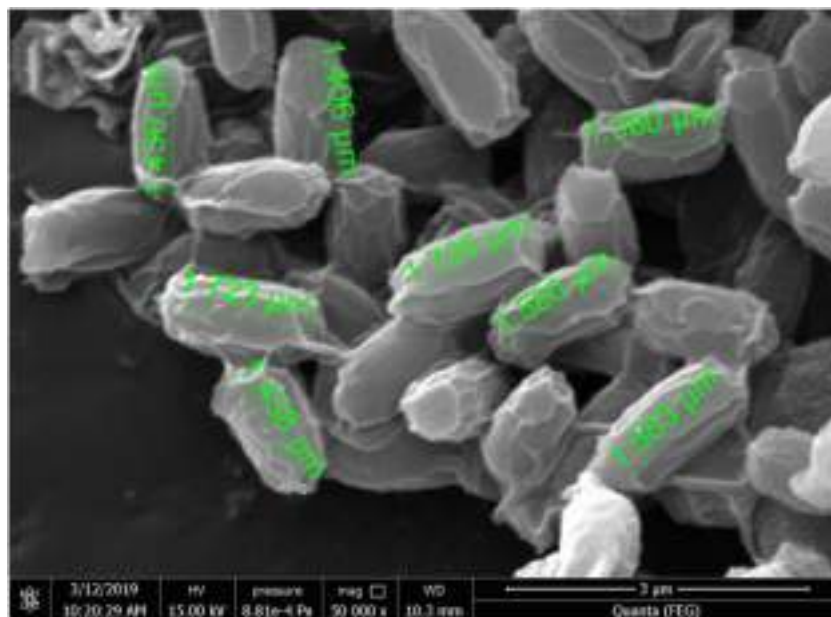


Fig. 2. Visualization of the isolated strain BPW19 under ESEM at 50000X magnification.

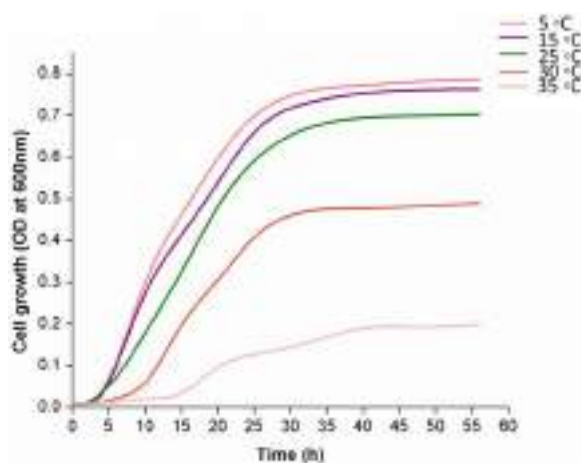


Fig. 3. The effect of temperature on cellular growth of BPW19 indicating the psychrotolerant nature of it.

was able to grow in a temperature range of 5 °C–35 °C it could be considered as a psychrotolerant bacteria [69]. Different strains of *Paenibacillus* had already been reported to be psychrophilic growing at extremely low-temperature conditions. Strains of *Paenibacillus* were isolated from the active permafrost layer of Alaska while another strain from the same family was isolated from chilled ready to eat meals and could sustain lower temperatures of about 7 °C [69–71]. Some other strains were also isolated from soil with their ability to grow at temperatures between 4 °C and 25 °C which is comparable with the isolated strain of the study BPW19 which also exhibits similar temperature range for effective growth [72].

3.4. Biomass production optimization

Based on CCD modeling, a total of 20 runs of the different combination was suggested by the software. The obtained biomass along with the run combinations have been represented in Table 3. The cubic model suggested by the software for cell growth was represented by Eq. (2). The difference between the adjusted and

predicted R^2 value was obtained as 0.0451 which is less than 0.2 and the overall R^2 value was determined as 0.9874. These statistics signified the good fit of the model. The ANOVA analysis (Tables 4 and 5) also suggested the model is signified with considerable F and p values and lack of fit was also found non-significant [43].

$$\text{Biomass} = 0.0951 - 0.0006A + 0.0056B + 0.014C - 0.0177AB - 0.0055AC + 0.0013BC + 0.0162A^2 + 0.0043B^2 - 0.0052C^2 - 0.005ABC + 0.0396A^2B - 0.0252A^2C - 0.0232AB^2 \quad (2)$$

where A, B, and C are temperature, pH, and inoculum percentage, respectively.

The model suggested that the pH and inoculum percentage had a positive impact whereas temperature had a negative impact on cellular growth (Fig. 4). According to the model, the preference of low temperature was found collinear with the psychrophilic character of PW19. But maintaining a lower temperature in the bioreactor makes the whole process exothermic but to support that refrigeration would be required [73]. Hence maintaining such low temperatures for industrial production will require energy consumption and incur operational and maintenance costs. The increased amount of biomass obtained at low temperature may not be sufficient to support the elevated process cost. Moreover, a low-temperature process is well known for slow bacterial growth rate, even for psychrophilic bacteria [74]. Hence lowering the temperature will increase operation time to obtain the maximum cell growth which is also not accepted in industrial-scale processes. So the optimum temperature was considered 25 °C which was found sufficient to support cell growth. The acceptance of the model was tested by the run suggested by the software with temperature 25 °C, pH 8, and inoculum percentage of 2.25 %. The predicted value of biomass was 0.19 g. The experimental result obtained was 0.18 g which confirmed the difference between the predicted and experimental value is only 5.85 % which is significantly low.

3.5. Pigment purification and yield

After the sonication process, the intracellular pigment was dissolved completely in methanol. The solution was further considered for TLC analysis which revealed two different bands using a mobile phase of ethanol and chloroform in 1:4 (v/v)

Table 3Experimental run combination of different process parameters for biomass production optimization of *Paenibacillus* sp. following CCD.

No.	Temperature (°C)	pH	Inoculum percentage (%)	Response : Biomass (g/L)
1	25	8	3.5	0.19
2	31	7	2.5	0.10
3	37	6	3.5	0.06
4	31	7	2.5	0.08
5	37	6	1.5	0.08
6	41.09	7	2.5	0.14
7	37	8	1.5	0.12
8	25	6	1.5	0.09
9	31	7	2.5	0.10
10	20.91	7	2.5	0.14
11	31	7	4.18	0.10
12	31	7	2.5	0.09
13	25	6	3.5	0.07
14	31	7	0.82	0.06
15	25	8	1.5	0.19
16	31	5.32	2.5	0.12
17	31	7	2.5	0.10
18	37	8	3.5	0.08
19	31	8.68	2.5	0.10
20	31	7	2.5	0.10

Table 4

ANOVA analysis obtained from the model suggested by software for the optimization of pigment production.

Source	Sum of Squares	df	Mean Square	F-value	p-value	
Model	0.0236	13	0.0018	36.12	0.0001	Significant
A-Temperature	2.000E-06	1	2.000E-06	0.0397	0.8486	
B-pH	0.0002	1	0.0002	3.58	0.1072	
C-Inoculum	0.0011	1	0.0011	21.93	0.0034	
AB	0.0025	1	0.0025	50.05	0.0004	
AC	0.0002	1	0.0002	4.81	0.0709	
BC	0.0000	1	0.0000	0.2482	0.6361	
A ²	0.0038	1	0.0038	74.83	0.0001	
B ²	0.0003	1	0.0003	5.36	0.0599	
C ²	0.0004	1	0.0004	7.80	0.0315	
ABC	0.0002	1	0.0002	3.97	0.0933	
A ² B	0.0052	1	0.0052	103.44	< 0.0001	
A ² C	0.0021	1	0.0021	41.86	0.0006	
AB ²	0.0018	1	0.0018	35.28	0.0010	
AC ²	0.0000	0				
B ² C	0.0000	0				
BC ²	0.0000	0				
A ³	0.0000	0				
B ³	0.0000	0				
C ³	0.0000	0				
Residual	0.0003	6	0.0001			
Lack of Fit	7.325E-06	1	7.325E-06	0.1242	0.7389	not significant
Pure Error	0.0003	5	0.0001			
Cor Total	0.0239	19				

Table 5

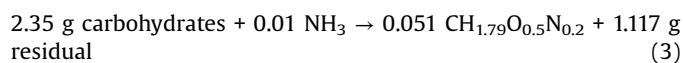
Fit statistics of the model suggested for optimization of pigment production.

Std. Dev.	0.0071	R ²	0.99
Mean	0.11	Adjusted R ²	0.96
C.V. %	6.72	Predicted R ²	0.92
		Adeq Precision	21.82

signifying the presence of two different chemicals in the crude pigment. The major pink band was observed to have an R_f value of 0.92, where the solvent front was 1.9 cm and the pigment front was 1.75 cm at around 30 °C. The purified pigment was obtained through column chromatography after collecting elutes of the major band considering similar R_f values and dried for further confirmatory analysis.

After 4 days of incubation in bioreactor maintaining the optimized culture conditions, 2.5 L of cell culture broth produced

around 3.14 g of dry cell mass. Considering R-2A broth contains 2.36 g/L of carbohydrates and 0.17 g/L of ammonia (a simplest representable form of nitrogen source) the stoichiometric equation, Eq. (3) was produced taking 1 L basis to represent biomass production during the process.



Where $\text{CH}_{1.79}\text{O}_{0.5}\text{N}_{0.2}$ is a universal bacterial biomass representation [43].

This inferred a net biomass yield of 0.35 g of dry biomass/g of carbohydrate. From the obtained 3.14 g of biomass, 0.17 g of crude pigment was recovered following the solvent extraction process. This indicated that the crude pigment was 5.41 % of the biomass by proportion. This solvent extraction process can be represented by the stoichiometric equation, Eq. (4) which was also prepared considering a 1 L basis.

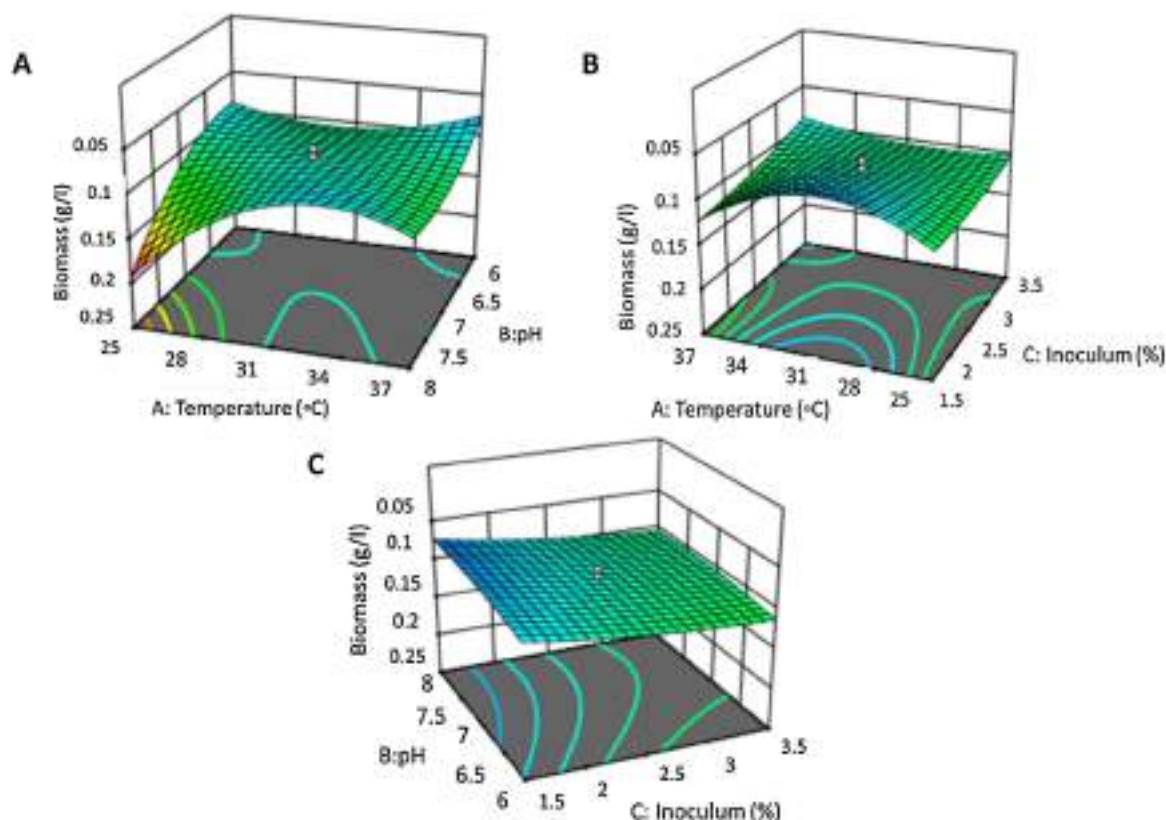


Fig. 4. Contour Plots of interaction between three factors considered during optimisation Temperature, pH and Inoculum (%); (A) Interaction between temperature and pH; (B) Interaction between temperature and inoculum %; (C) Interaction between pH and inoculum %.

$0.051 \text{ CH}_{1.79}\text{O}_{0.5}\text{N}_{0.2} \rightarrow 0.066 \text{ g crude pigment} + 1.186 \text{ g cell debris}$ (4)

The obtained crude pigment was further purified using column chromatography and around 0.1 g of purified pigment compounds was obtained from 0.17 g of crude pigment. This resulted in 57.80 % of the crude pigment if purified as the final pigment compound. This purification process can be expressed stoichiometrically as Eq. (5). The net yield of purified pigment was 3.06 % from biomass.

$0.07 \text{ g crude pigment} \rightarrow 0.03 \text{ g purified pigments} + 0.03 \text{ g contaminants}$ (5)

The net yield of purified pigment for this process was obtained as 0.1 g from 2.5 L of bacterial culture. The yield obtained for the pigment in this study is comparable with yields reported in recent literature for intracellular pigment isolation from bacteria. The recorded yield in this study was 68 mg/L of crude pigment from the BPW19 strain by the solvent extraction method. This result is 3.5 times higher than the yield of 18.90 mg/L reported for a strain of *D. violaceinigr* [79] and 4.5 times higher than the yield of 15 mg/L

reported for *Formosa* sp. [88]. The optimization of process conditions for maximum biomass production led to the higher yield in our study as compared to the other reports. In another report, violacein pigment was produced by *Janthinobacterium* species and optimization of growth conditions was done followed by pigment isolation using solvent extraction method [78]. The obtained yield in the report was 77 mg/L which is comparable with the yield results of the current study.

The higher yield observed in our study was due to the pigment extraction after optimizing the parameters for maximum biomass production followed by the use of only a single-step purification process of the crude pigment. Therefore the production and extraction of the intracellular pigments from BPW19 through solvent extraction provided a higher yield with no energy consumption as compared to other extraction processes, making it a cost-effective approach. Another study on the extraction of intracellular yellow pigment from coral-associated bacteria *Vibrio owensii* TNKJ.CR.24–7 reported a yield of about 1.14 % when isolated with 1-butanol which was comparable with BPW19 strain of this study provided a yield of 3.06 % after purification stating a

Table 6
Comparative representation of pigment yield from other bacterial sources.

Pigment	Type	Species	Pigment isolation method	Yield	References
Indochrome type blue pigment	Extracellular	<i>Pseudarthrobacter</i> sp.	Solid-phase extraction	2.5 g/L	[41]
Carotenoid like pigment	Intracellular	<i>Arthrobacter</i> sp.	Solvent extraction	0.84 g/L	[77]
Violacein	Intracellular	<i>Janthinobacterium</i> sp.	Solvent extraction	77 mg/L crude	[78]
Violacein	Intracellular	<i>Duganella violaceinigr</i> str. NI28	Solvent extraction	18.9 mg/L crude	[79]
Prodigiosin	Intracellular	<i>Serratia marcescens</i>	Ultrasonication	$2.54 \pm 0.41 \text{ mg/mL}$	[80]
			Freeze-thawing	$0.06 \pm 0.02 \text{ mg/mL}$	
			Homogenization	$0.49 \pm 0.10 \text{ mg/mL}$	
Pink pigment	Intracellular	<i>Paenibacillus</i> sp.	Solvent extraction	3.06 g/100 g of biomass	This study

relatively higher yield [76]. Comparative representation of the pigment yield of this study along with other recent works had been discussed in Table 6 [41,77–80].

3.6. Antibacterial assay of crude pigment

The solvent extraction process produced crude pigment which was further evaluated for its antibacterial property. The crude pigment showed antibacterial property against Gram-negative test strains. Growth inhibition zone of about 2.5 mm was obtained against *E. coli* whereas 3.1 mm and 2.9 mm were observed against *Enterobacter* sp. and *Klebsiella* sp., respectively. No antibacterial effect was observed against the Gram-positive bacteria *B. subtilis*. Hence the pigment was found to be effective against Gram-negative bacterial strains. Some reported bacterial pigments exhibited similar kinds of antibacterial activity which include prodigiosin produced by *Serratia* sp. PDGS 120915, phycocyanin pigment by *Pseudomonas aeruginosa*, etc [31,75]. Although no strain of *Paenibacillus* genus was reported with pigment production, however, some strains like *Paenibacillus polymyxa* and *Paenibacillus thiaminolyticus* were reported to produce antimicrobial substances comprised of bacteriocins, lipopeptides, enzymes, and different volatile organic compounds [81].

3.7. GC–MS and NMR analysis

The GC–MS analysis of crude pigment indicated the presence of a variety of complex components (Fig. 5a). Among them, the main four dominating compounds were identified as dotriacontane (16.72 min), 3,7 dimethyl 7 octanal (16.83 min), 1-eicosene (17.17 min) and erucic acid (17.19 min) with percentage area of 1.39 %, 23.66 %, 22.87 %, and 12.75 %, respectively (Fig. 5b). Among these identified compounds, dotriacontane is a long chain hydrocarbon having 32 carbon atoms. It had been reported with antibacterial, antioxidant, and antispasmodic activity. On the other hand, compound 1-eicosene is a suitable anticancer agent and possesses immunosuppressive activity. It also acts as a radical scavenger to reduce the chemical stress.

NMR spectrum analysis was used to identify the component in the purified pigment compound. The ^{13}C analysis confirms the presence of 1 carbonyl compound, two double-bonded carbons (sp^2), and 20 other (sp^3) carbons (Fig. 6a). Proton count also confirmed the presence of a carboxyl group, an internal double bond, and a total of forty-two hydrogen (Fig. 6b). The NMR spectrum analysis combined with the GC–MS report, the component of the purified pigment was identified as erucic acid (Fig. 7). Erucic acid is effectively used as a surfactant in various oleochemical industries and is one of the fundamental compounds in hydraulic fluids [82]. It is also used for the production of lubricants, detergents, plastics, resins, and lacquers [83]. The application of high erucic acid contained oil as cutting oil for metals paves finds its utilization in the metallurgical industries [84].

4. Application of the present work

Pigment production from bacterial sources is beneficial in terms of large scale production with low generation time and presence of different biological compounds like antioxidants and antimicrobials along with biocompatibility, less toxicity, economic and eco-friendly. The present work reported pigment production from a strain of the *Paenibacillus* genus for the first time. The intracellular pigment was extracted using solvent extraction after sonication and heat mediated cell disruption. The solvent extraction process aids in a less expensive pigment production with no energy requirement. Bacterial pigment allows very little amounts of waste generation and also reduces the cost of chief substrates for the production line. The purified compound from the pigment was identified as erucic acid which has its application in oleochemical industries as surfactants and also used in the production of lubricants, detergents, plastics, resins, and lacquers [83]. The compound is also regarded as essential in the metallurgical industries as high erucic acid contained oil is used as cutting oil for metal paves [84]. It is also one of the major compounds used in hydraulic fluids and is considered important in the automobile industries [82]. Other natural sources of erucic acid

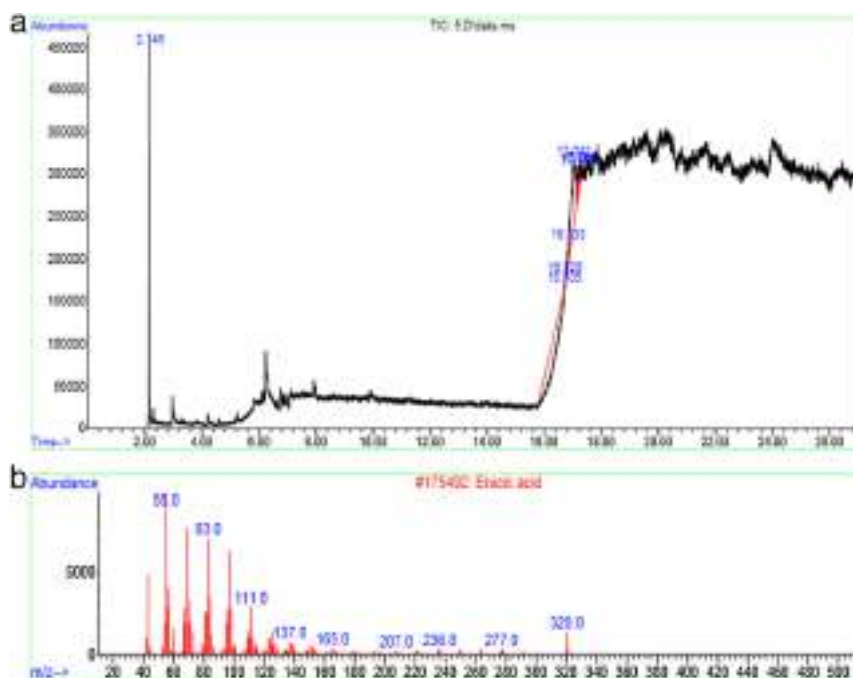


Fig. 5. a The GC–MS chromatogram of the crude pigment. b The GC–MS chromatogram showing the presence of erucic acid as one of the compounds in the crude pigment.

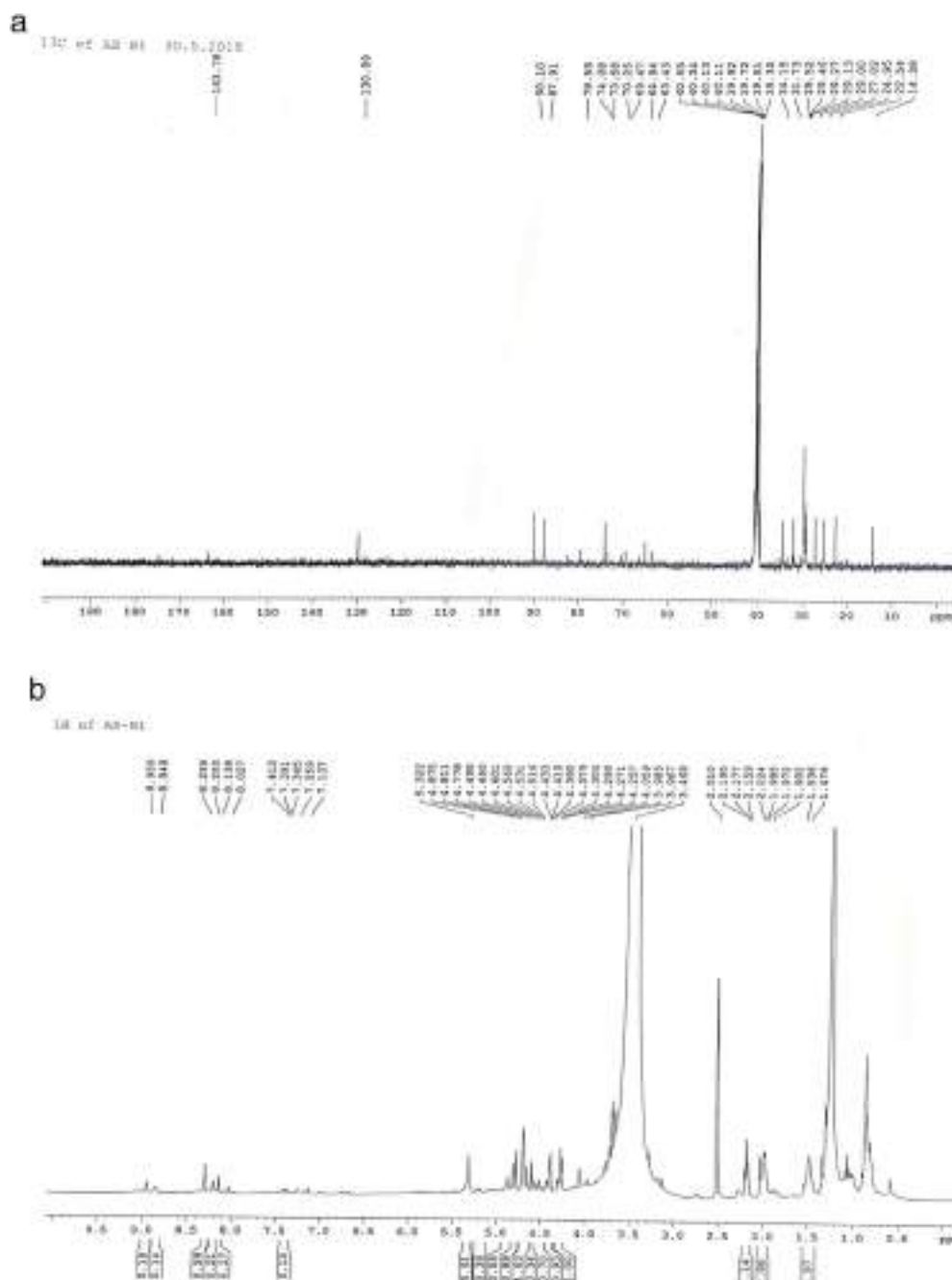


Fig. 6. a The ^{13}C nuclear magnetic resonance spectrum for the purified pigment fraction of the major band. b The ^1H nuclear magnetic resonance spectrum for the purified pigment fraction of the major band.



Fig. 7. Structure of erucic acid obtained as the major product after purification from pigment produced by isolated strain BPW19.

include plants of *Brassicaceae* family, particularly rapeseed and mustard. Since plants have higher generation time, industrial use of erucic acid from plants would exhaust the inflow of chief substrates thereby increasing the overall cost of the production system. Plant source for erucic acid also involves other factors like labor cost, seasonality, and large cultivable land. Hence the bacterial source of the compound makes it a significant alternative to avoid the limitations. Apart from these, industrial bacterial culture minimizes the cost of pre-processing, unlike plants that require intermediate steps of chopping, processing, and filtration for the extraction of the compound thus reducing the overall cost. The pigment produced alongside in the bacterial source also serves as a beneficial and commercial by-product.

5. Conclusion

The BPW19 strain was successfully isolated from wastewater and was found to be a member of the *Paenibacillaceae* family. The strain showed psychrotolerant nature, implying its ability to grow both in low and moderate temperature. Since low temperature operations are costlier and are difficult to maintain, giving priority to this fact, the biomass production was optimized at moderate temperature to ensure the ease of the operation. The intercellular bacterial pigment was successfully extracted by sonication assisted solvent extraction using slightly polar solvent indicating the amphiphobic nature of the crude pigment. The crude pigment exhibited antibacterial activity especially against different gram negative bacterial strain enlightening its probable application as an antibacterial substance. The GC-MS analysis detected four major compounds in the crude pigment, namely, dotriacontane; 3,7 dimethyl 7 octanal; 1-eicosene and erucic acid. After column chromatography, the crude pigment was purified and the purified compound was detected as erucic acid by NMR analysis. Erucic acid has many applications in the oleochemical, metallurgical, and automobile industries. This study has established BPW19 as a cost-effective source of a bacterial pigment that may have diverse industrial applications and large scale production of the pigment with optimization and cost efficiency calculation can open up new opportunities for commercialization of the pigment.

Declaration of Competing Interest

The authors report no declarations of interest.

Acknowledgment

The authors would like to acknowledge the National Institute of Technology Rourkela for providing a suitable research environment and the required technical facilities.

Appendix A. Supplementary data

Supplementary material related to this article can be found, in the online version, at doi:<https://doi.org/10.1016/j.btre.2021.e00592>.

References

- [1] M. Sabet, M. Salavati-Niasari, O. Amiri, Using different chemical methods for deposition of CdS on TiO₂ surface and investigation of their influences on the dye-sensitized solar cell performance, *Electrochim. Acta* 117 (2014) 504–520, doi:<http://dx.doi.org/10.1016/j.electacta.2013.11.176>.
- [2] G. Bisht, S. Srivastava, R. Kulshreshtha, A. Sourirajan, D.J. Baulmer, K. Dev, Applications of red pigments from psychrophilic *Rhodonellum psychrophilum* GL8 in health, food and antimicrobial finishes on textiles, *Process Biochem.* 94 (2020) 15–29, doi:<http://dx.doi.org/10.1016/j.procbio.2020.03.021>.
- [3] Dyes and pigments market size, Share & Trends Analysis Report by Product (dyes (reactive, Vat, Acid, Direct, Disperse), Pigment (organic, Inorganic)), by Application, by Region, and Segment Forecasts, 2020 – 2027, Market Report Analysis, (2020) Report ID: GVR-1-68038-545-548. Accessed 24 August 2020.
- [4] P. Bakthavachalu, S.M. Kannan, M.W. Qoronfle, Food color and autism: a meta-analysis, in: M.M. Essa, M.W. Qoronfle (Eds.), *Personalized Food Intervention and Therapy for Autism spectrum Disorder Management*, Springer, Cham, 2020, pp. 481–504, doi:<http://dx.doi.org/10.1007/978-3-030-30402-7>.
- [5] A. Tkaczyk, K. Mitrowska, A. Posyniak, Synthetic organic dyes as contaminants of the aquatic environment and their implications for ecosystems: a review, *Sci. Total Environ.* 717 (2020) 137222, doi:<http://dx.doi.org/10.1016/j.scitotenv.2020.137222>.
- [6] Y. Orooji, M. Ghanbari, O. Amiri, M. Salavati-Niasari, Facile fabrication of silver iodide/graphitic carbon nitride nanocomposites by notable photo-catalytic performance through sunlight and antimicrobial activity, *J. Hazard. Mater.* 389 (2020) 122079, doi:<http://dx.doi.org/10.1016/j.jhazmat.2020.122079>.
- [7] M.H. Khorasanizadeh, R. Monsef, O. Amiri, M. Amiri, M. Salavati-Niasari, Sonochemical-assisted route for synthesis of spherical shaped holmium vanadate nanocatalyst for polluted waste water treatment, *Ultrason. Sonochem.* 58 (2019) 104686, doi:<http://dx.doi.org/10.1016/j.ultsonch.2019.104686>.
- [8] A.J. Sisi, M. Fathinia, A. Khataee, Y. Orooji, Systematic activation of potassium peroxydisulfate with ZIF-8 via sono-assisted catalytic process: mechanism and ecotoxicological analysis, *J. Mol. Liq.* 308 (2020) 113018, doi:<http://dx.doi.org/10.1016/j.molliq.2020.113018>.
- [9] M. Salavati-Niasari, D. Ghanbari, M.R. Loghman-Estarki, Star-shaped PbS nanocrystals prepared by hydrothermal process in the presence of thioglycolic acid, *Polyhedron* 35 (2012) 149–153, doi:<http://dx.doi.org/10.1016/j.poly.2012.01.010>.
- [10] P. Mehdizadeh, Y. Orooji, O. Amiri, M. Salavati-Niasari, H. Moayed, Green synthesis using cherry and orange juice and characterization of TbFeO₃ ceramic nanostructures and their application as photocatalysts under UV light for removal of organic dyes in water, *J. Clean. Prod.* 252 (2020) 119765, doi:<http://dx.doi.org/10.1016/j.jclepro.2019.119765>.
- [11] M. Dastkhoo, M. Ghaedi, A. Asfaram, R. Jannesar, F. Sadeghfar, Magnetic based nanocomposite sorbent combination with ultrasound assisted for solid-phase microextraction of Azure II in water samples prior to its determination spectrophotometric, *J. Colloid Interface Sci.* 513 (2018) 240–250, doi:<http://dx.doi.org/10.1016/j.jcis.2017.11.031>.
- [12] A. Asfaram, M. Ghaedi, H. Javadian, A. Goudarzi, Cu- and S- @SnO₂ nanoparticles loaded on activated carbon for efficient ultrasound assisted dispersive μ SPE-spectrophotometric detection of quercetin in *Nasturtium officinale* extract and fruit juice samples: CCD-RSM design, *Ultrason. Sonochem.* 47 (2018) 1–9, doi:<http://dx.doi.org/10.1016/j.ultsonch.2018.04.008>.
- [13] M. Salavati-Niasari, Synthesis and characterization of host (nanodimensional pores of zeolite-Y)-guest [unsaturated 16-membered Octaaza-macrocyclic Manganese(II), Cobalt(II), Nickel(II), Copper(II), and Zinc(II) complexes] nanocomposite Materials, *Chem. Lett.* 34 (2005) 1444–1445, doi:<http://dx.doi.org/10.1246/cl.2005.1444>.
- [14] M. Ghasemi, A. Khataee, P. Gholami, R. Soltani, A. Hassani, Y. Orooji, In-situ electro-generation and activation of hydrogen peroxide using a CuFeNLDH-CNTs modified graphite cathode for degradation of cefazolin, *J. Environ. Manage.* 267 (2020) 110629, doi:<http://dx.doi.org/10.1016/j.jenvman.2020.110629>.
- [15] R. Monsef, M. Ghiyasiyan-Arani, M. Salavati-Niasari, Application of ultrasound-aided method for the synthesis of NdVO₄ nano-photocatalyst and investigation of eliminate dye in contaminant water, *Ultrason. Sonochem.* 42 (2018) 201–211, doi:<http://dx.doi.org/10.1016/j.ultsonch.2017.11.025>.
- [16] Y. Orooji, R. Mohassel, O. Amiri, A. Sobhani, M. Salavati-Niasari, Gd₂ZnMnO₆/ZnO nanocomposites: green sol-gel auto-combustion synthesis, characterization and photocatalytic degradation of different dye pollutants in water, *J. Alloys Compd.* 835 (2020) 155240, doi:<http://dx.doi.org/10.1016/j.jallcom.2020.155240>.
- [17] R. Monsef, M. Ghiyasiyan-Arani, M. Salavati-Niasari, Utilizing of neodymium vanadate nanoparticles as an efficient catalyst to boost the photocatalytic water purification, *J. Environ. Manage.* 230 (2019) 266–281, doi:<http://dx.doi.org/10.1016/j.jenvman.2018.09.080>.
- [18] F. Davar, M. Salavati-Niasari, Synthesis and characterization of spinel-type zinc aluminate nanoparticles by a modified sol-gel method using new precursor, *J. Alloys Compd.* 509 (2011) 2487–2492, doi:<http://dx.doi.org/10.1016/j.jallcom.2010.11.058>.
- [19] Y. Orooji, A. Alizadeh, E. Ghasali, M.R. Derakhshandeh, M. Alizadeh, M. Shahedi Asl, T. Ebadzadeh, Co-reinforcing of mullite-TiN-CNT composites with ZrB₂ and TiB₂ compounds, *Ceram. Int.* 45 (2019) 20844–20854, doi:<http://dx.doi.org/10.1016/j.ceramint.2019.07.072>.
- [20] M. Salavati-Niasari, M. Loghman-Estarki, F. Davar, Controllable synthesis of nanocrystalline CdS with different morphologies by hydrothermal process in the presence of thioglycolic acid, *Chem. Eng. J.* 145 (2008) 346–350, doi:<http://dx.doi.org/10.1016/j.cej.2008.08.040>.
- [21] F. Mohandes, F. Davar, M. Salavati-Niasari, Magnesium oxide nanocrystals via thermal decomposition of magnesium oxalate, *J. Phys. Chem. Solids* 71 (2010) 1623–1628, doi:<http://dx.doi.org/10.1016/j.jpcs.2010.08.014>.
- [22] M. Salavati-Niasari, Ship-in-a-bottle synthesis, characterization and catalytic oxidation of styrene by host (nanopores of zeolite-Y)/guest ([bis(2-hydroxyanil)acetylacetonato manganese(III)]) nanocomposite materials (HGNN), *Microporous Mesoporous Mater.* 95 (2006) 248–256, doi:<http://dx.doi.org/10.1016/j.micromeso.2006.05.025>.
- [23] A. Asfaram, M. Ghaedi, M.K. Purkait, Novel synthesis of nanocomposite for the extraction of Sildenafil Citrate (Viagra) from water and urine samples: process screening and optimization, *Ultrason. Sonochem.* 38 (2017) 463–472, doi:<http://dx.doi.org/10.1016/j.ultsonch.2017.03.045>.
- [24] A. Asfaram, E. Dil, P. Arabkhani, F. Sadeghfar, M. Ghaedi, Magnetic Cu: CuO-GO nanocomposite for efficient dispersive micro-solid phase extraction of polycyclic aromatic hydrocarbons from vegetable, fruit, and environmental water samples by liquid chromatographic determination, *Talanta* 218 (2020) 121131, doi:<http://dx.doi.org/10.1016/j.talanta.2020.121131>.
- [25] A. Sarkar, D. Sarkar, K. Poddar, Nanotoxicity: sources and effects on environment, in: R. Prasad (Ed.), *Microbial Nanobionics*, Springer, Cham, 2019, pp. 169–179, doi:<http://dx.doi.org/10.1007/978-3-030-16534-5>.
- [26] A. Sarkar, D. Sarkar, K. Poddar, Plant metabolites as new leads to drug discovery: approaches and challenges, in: M.K. Swamy, J.K. Patra, G.R. Rudramurthy (Eds.), *Medicinal Plants: Chemistry, Pharmacology, and Therapeutic Applications*, CRC Press, Boca Raton, 2019, pp. 61–69, doi:<http://dx.doi.org/10.1201/9780429259968-5>.

- [27] N. Gupta, K. Poddar, D. Sarkar, N. Kumari, B. Padhan, A. Sarkar, Fruit waste management by pigment production and utilization of residual as bioadsorbent, *J. Environ. Manage.* 244 (2019) 138–143, doi:<http://dx.doi.org/10.1016/j.jenvman.2019.05.055>.
- [28] S. Sánchez-Muñoz, G. Mariano-Silva, M.O. Leite, F.B. Mura, M.L. Verma, S.S. da Silva, A.K. Chandel, Production of fungal and bacterial pigments and their applications, in: M.L. Verma, A.K. Chandel (Eds.), *Biotechnological Production of Bioactive Compounds*, Elsevier, 2020, pp. 327–361, doi:<http://dx.doi.org/10.1016/C2018-0-02574-8>.
- [29] E. Setiyono, T.H.P. Brotsudarmo, D. Pringgenies, M.N.U. Prihastyanti, Y. Shioi, Analysis of β -cryptoxanthin from yellow pigmented marine bacterium *erythrobacter* sp. kj5, *IOP Conf. Ser. Earth Environ. Sci.* 246(2019) 012004.
- [30] S. PB, A. JC, J. Rathinamala, S. Jayashree, The role of red pigment prodigiosin from bacteria of earthworm gut as an anticancer agent, *J. Microbiol. Biotechnol. Food Sci.* 4 (2019) 246–251, doi:<http://dx.doi.org/10.15414/jmbfs.2014-15.4.3.246-251>.
- [31] S. DeBritto, T.D. Gajbar, P. Satapute, L. Sundaram, R.Y. Lakshmikantha, S. Jogaiah, S.I. Ito, Isolation and characterization of nutrient dependent pyocyanin from *Pseudomonas aeruginosa* and its dye and agrochemical properties, *Sci. Rep.* 10 (2020) 1–12, doi:<http://dx.doi.org/10.1038/s41598-020-58335-6>.
- [32] N.E.A. El-Naggar, M.H. Hussein, A.A. El-Sawah, Bio-fabrication of silver nanoparticles by phycocyanin, characterization, in vitro anticancer activity against breast cancer cell line and in vivo cytotoxicity, *Sci. Rep.* 7 (2017) 10844, doi:<http://dx.doi.org/10.1038/s41598-017-11121-3>.
- [33] P. Hernández-Velasco, I. Morales-Atilano, M. Rodríguez-Delgado, J.M. Rodríguez-Delgado, D. Luna-Moreno, F.G. Ávalos-Alanis, J.F. Villarreal-Chiu, Photoelectric evaluation of dye-sensitized solar cells based on prodigiosin pigment derived from *Serratia marcescens* 11E, *Dye. Pigment.* 177 (2020) 108278, doi:<http://dx.doi.org/10.1016/j.dyepig.2020.108278>.
- [34] F.A. Venegas, G. Köllisch, K. Mark, W.E. Diederich, A. Kaufmann, S. Bauer, M. Chavarría, J.J. Araya, A.J. García-Piñeres, The bacterial product violacein exerts an immunostimulatory effect via TLR8, *Sci. Rep.* 9 (2019) 1–17, doi:<http://dx.doi.org/10.1038/s41598-019-50038-x>.
- [35] C.K. Venil, Z.A. Zakaria, W.A. Ahmad, Optimization of culture conditions for flexirubin production by *Chrysobacterium artocarp* CECT 8497 using response surface methodology, *Acta Biochim. Pol.* 62 (2015) 185–190.
- [36] M. Assia, A. Hasnaa, M. Sara, M. Jamal, M. Mohammed, Physico-chemical characterization of a pink red-like pigments produced by five new bacterial soil strains identified as *Streptomyces coelicolor*, *Am. J. Microbiol. Res.* 6 (2018) 67–72, doi:<http://dx.doi.org/10.12691/ajmr-6-3-1>.
- [37] N. Órdenes-Aenishanslins, G. Anziani-Ostuni, M. Vargas-Reyes, J. Alarcón, A. Tello, J.M. Pérez-Donoso, Pigments from UV-resistant Antarctic bacteria as photosensitizers in dye sensitized solar cells, *J. Photochem. Photobiol. B* 162 (2016) 707–714, doi:<http://dx.doi.org/10.1016/j.jphotobiol.2016.08.004>.
- [38] D. Asker, Isolation and characterization of a novel, highly selective astaxanthin-producing marine bacterium, *J. Agric. Food Chem.* 65 (2017) 9101–9109, doi:<http://dx.doi.org/10.1021/acs.jafc.7b03556>.
- [39] T. Kimura, W. Fukuda, T. Sanada, T. Imanaka, Characterization of water-soluble dark-brown pigment from Antarctic bacterium, *Lysobacter oligotrophicus*, *J. Biosci. Bioeng.* 120 (2015) 58–61, doi:<http://dx.doi.org/10.1016/j.jbiosc.2014.11.020>.
- [40] P.S. Selvi, P. Iyer, Isolation and characterization of pigments from marine soil microorganisms, *IJLSSR* 4 (2018) 2003–2011, doi:<http://dx.doi.org/10.21276/ijlssr.2018.4.5.7>.
- [41] S. Finger, F.A. Godoy, G. Wittwer, C.P. Aranda, R. Calderón, C.D. Miranda, Purification and characterization of indochrome type blue pigment produced by *Pseudarthrobacter* sp. 34LCH1 isolated from Atacama desert, *J. Ind. Microbiol. Biot.* 46 (2019) 101–111, doi:<http://dx.doi.org/10.1007/s10295-018-2088-3>.
- [42] T.R. Silva, R. Canela-Garayoa, J. Eras, M.V. Rodrigues, F.N. dos Santos, M.N. Eberlin, I.A. Neri-Numa, G.M. Pastore, R.S. Tavares, H.M. Debonsi, L.R. Cordeiro, Pigments in an iridescent bacterium, *Cellulophaga fucicola*, isolated from Antarctica, *Antonie Van Leeuwenhoek* 112 (2019) 479–490, doi:<http://dx.doi.org/10.1007/s10482-018-1179-5>.
- [43] D. Sarkar, S. Prajapati, K. Poddar, A. Sarkar, Production of ethanol by *Enterobacter* sp. EtK3 during fruit waste biotransformation, *Int. Biodeterior. Biodegrad.* 145 (2019) 104795, doi:<http://dx.doi.org/10.1016/j.ibiod.2019.104795>.
- [44] B. Ramola, V. Kumar, M. Nanda, Y. Mishra, T. Tyagi, A. Gupta, N. Sharma, Evaluation, comparison of different solvent extraction, cell disruption methods and hydrothermal liquefaction of *Oedogonium* macroalgae for biofuel production, *Biotechnol. Rep.* 22 (2019), doi:<http://dx.doi.org/10.1016/j.btre.2019.e00340>.
- [45] M.A. Dar, A.A. Shaikh, K.D. Pawar, R.S. Pandit, Exploring the gut of *Helicoverpa armigera* for cellulose degrading bacteria and evaluation of a potential strain for lignocellulosic biomass deconstruction, *Process Biochem.* 73 (2018) 142–153, doi:<http://dx.doi.org/10.1016/j.procbio.2018.08.001>.
- [46] D. Sarkar, K. Gupta, K. Poddar, R. Biswas, A. Sarkar, Direct conversion of fruit waste to ethanol using marine bacterial strain *Citrobacter* sp. E4, *Process Saf. Environ.* 128 (2019) 203–210, doi:<http://dx.doi.org/10.1016/j.psep.2019.05.051>.
- [47] K. Poddar, D. Sarkar, A. Sarkar, Construction of potential bacterial consortia for efficient hydrocarbon degradation, *Int. Biodeterior. Biodegrad.* 144 (2019) 104770, doi:<http://dx.doi.org/10.1016/j.ibiod.2019.104770>.
- [48] B.Y. Gül, I. Koyuncu, Assessment of new environmental quorum quenching bacteria as a solution for membrane biofouling, *Process Biochem.* 61 (2017) 137–146, doi:<http://dx.doi.org/10.1016/j.procbio.2017.05.030>.
- [49] E. Vila, D. Hornero-Méndez, G. Azziz, C. Lareo, V. Saravia, Carotenoids from heterotrophic bacteria isolated from Fildes Peninsula, King George Island, Antarctica, *Biotechnol. Rep.* 21 (2019), doi:<http://dx.doi.org/10.1016/j.btre.2019.e00306>.
- [50] U. Dey, S. Chatterjee, N.K. Mondal, Isolation and characterization of arsenic-resistant bacteria and possible application in bioremediation, *Biotechnol. Rep.* 10 (2016) 1–7, doi:<http://dx.doi.org/10.1016/j.btre.2016.02.002>.
- [51] I. Kim, J. Kim, G. Chhetri, T. Seo, *Flavobacterium humi* sp. nov., a flexirubin-type pigment producing bacterium, isolated from soil, *J. Microbiol.* 57 (2019) 1079–1085, doi:<http://dx.doi.org/10.1016/j.procbio.2017.05.003>.
- [52] B. Biswas, B. Sarkar, S. McClure, R. Naidu, Modified osmium tracer technique enables precise microscopic delineation of hydrocarbon-degrading bacteria in clay aggregates, *Environ. Technol. Innov.* 7 (2017) 12–20, doi:<http://dx.doi.org/10.1016/j.eti.2016.11.002>.
- [53] N.M. Elkenawy, A.S. Yassin, H.N. Elhifnawy, M.A. Amin, Optimization of prodigiosin production by *Serratia marcescens* using crude glycerol and enhancing production using gamma radiation, *Biotechnol. Rep.* 14 (2017) 47–53, doi:<http://dx.doi.org/10.1016/j.btre.2017.04.001>.
- [54] P. Kaur, G. Ghoshal, A. Jain, Bio-utilization of fruits and vegetables waste to produce β -carotene in solid-state fermentation: characterization and antioxidant activity, *Process Biochem.* 76 (2019) 155–164, doi:<http://dx.doi.org/10.1016/j.procbio.2018.10.007>.
- [55] D. Sarkar, S. Prajapati, K. Poddar, A. Sarkar, Ethanol production by *Klebsiella* sp. SWET4 using banana peel as feasible substrate, *Biomass Convers. Biorefin.* (2020) 1–13, doi:<http://dx.doi.org/10.1007/s13399-020-00880-1>.
- [56] G. Sharmila, C. Muthukumar, E. Suriya, R.M. Keerthana, M. Kamatchi, N.M. Kumar, T. Anbarasan, J. Jeyanthi, Ultrasound aided extraction of yellow pigment from *Tecoma castanifolia* floral petals: optimization by response surface method and evaluation of the antioxidant activity, *Ind. Crops Prod.* 130 (2019) 467–477, doi:<http://dx.doi.org/10.1016/j.indcrop.2019.01.008>.
- [57] J.W. Choi, J.P. Park, Water-soluble red pigment production by *Paecilomyces sinclairii* and biological characterization, *Biotechnol. Bioprocess Eng.* 23 (2018) 246–249, doi:<http://dx.doi.org/10.1007/s12257-018-0103-1>.
- [58] F. Meddeb-Mouelhi, J.K. Moisan, J. Bergeron, B. Daoust, M. Beauregard, Structural characterization of a novel antioxidant pigment produced by a photochromogenic *Microbacterium oxydans* strain, *Appl. Biochem. Biotechnol.* 180 (2016) 1286–1300, doi:<http://dx.doi.org/10.1007/s12010-016-2167-8>.
- [59] S.S. Narayani, S. Saravanan, S. Bharathiraja, S. Mahendran, Extraction, partially purification and study on antioxidant property of fucoxanthin from *Sargassum cinereum* J. Agardh, *J. Chem. Pharm. Res.* 8 (2016) 610–616.
- [60] S.S. Kharade, K.C. Samal, G.R. Rout, High performance thin layer chromatography fingerprint profile of rhizome extracts of five important *Curcuma* species, *Proc. Natl. Acad. Sci. India Sect. B Biol. Sci.* 87 (2017) 1335–1341, doi:<http://dx.doi.org/10.1007/s40011-016-0709-z>.
- [61] G. Mukherjee, S.K. Singh, Purification and characterization of a new red pigment from *Monascus purpureus* in submerged fermentation, *Process Biochem.* 46 (2011) 188–192, doi:<http://dx.doi.org/10.1016/j.procbio.2010.08.006>.
- [62] M. Numan, S. Bashir, R. Mumtaz, S. Tayyab, I. Ullah, A.L. Khan, Z.K. Shinwari, A. Al-Harrasi, Chemical profile and in-vitro pharmacological activities of yellow pigment extracted from *Arthrobacter gandavensis*, *Process Biochem.* 75 (2018) 74–82, doi:<http://dx.doi.org/10.1016/j.procbio.2018.08.033>.
- [63] G. Mohan, A.K.T. Thangappanpillai, B. Ramasamy, Antimicrobial activities of secondary metabolites and phylogenetic study of sponge endosymbiotic bacteria, *Bacillus* sp. at Agatti Island, Lakshadweep Archipelago, *Biotechnol. Rep.* 11 (2016) 44–52, doi:<http://dx.doi.org/10.1016/j.btre.2016.06.001>.
- [64] L. Zhou, T. Zhang, S. Tang, X. Fu, S. Yu, Pan-genome analysis of *Paenibacillus polymyxa* strains reveals the mechanism of plant growth promotion and biocontrol, *Antonie Van Leeuwenhoek* (2020) 1–20.
- [65] M. Wu, Y. Zong, W. Guo, G. Wang, M. Li, *Paenibacillus montanisol* sp. nov., isolated from mountain area soil, *Int. J. Syst. Evol. Microbiol.* 68 (2018) 3569–3575, doi:<http://dx.doi.org/10.1099/ijsem.0.003036>.
- [66] I.V. Yegorenkova, K.V. Tregubova, A.V. Schelud'ko, Motility in liquid and semisolid media of *Paenibacillus polymyxa* associative rhizobacteria differing in exopolysaccharide yield and properties, *Symbiosis* 74 (2018) 31–42, doi:<http://dx.doi.org/10.1007/s13199-017-0492-5>.
- [67] C.I. Lo, S.A. Sankar, B. Fall, B. Sambe-Ba, O. Mediannikov, C. Robert, N. Faye, B. Wade, D. Raoult, P.E. Fournier, F. Fenollar, High-quality genome sequence and description of *Paenibacillus dakarensis* sp. nov., *New Microbes New Infect.* 10 (2016) 132–141, doi:<http://dx.doi.org/10.1016/j.nmni.2016.01.011>.
- [68] S. Huecas, A.J. Canosa-Valls, L. Araújo-Bazán, F.M. Ruiz, D.V. Laurents, C. Fernández-Tornero, J.M. Andreu, Nucleotide-induced folding of cell division protein FtsZ from *Staphylococcus aureus*, *FEBS J.* (2020), doi:<http://dx.doi.org/10.1111/febs.15235>.
- [69] A.S. Panwar, D. Molpa, G.K. Joshi, Biotechnological potential of some cold-adapted bacteria isolated from North-Western Himalaya, *Microbiology* 88 (2019) 343–352, doi:<http://dx.doi.org/10.1134/S002626171903007X>.
- [70] H. Kim, A.K. Park, J.H. Lee, S.C. Shin, H. Park, H.W. Kim, PsEst3, a new psychrophilic esterase from the Arctic bacterium *Paenibacillus* sp. R4: crystallization and X-ray crystallographic analysis, *Acta Crystallogr. F* 74 (2018) 367–372, doi:<http://dx.doi.org/10.1107/S2053230X18007525>.
- [71] M. Helmond, M.N.N. Groot, H. van Bokhorst-van de Veen, Characterization of four *Paenibacillus* species isolated from pasteurized, chilled ready-to-eat meals, *Int. J. Food Microbiol.* 252 (2017) 35–41, doi:<http://dx.doi.org/10.1016/j.jfoodmicro.2017.04.008>.

- [72] S.H. Park, W. Yoo, C.W. Lee, C.S. Jeong, S.C. Shin, H.W. Kim, H. Park, K.K. Kim, T.D. Kim, J.H. Lee, Crystal structure and functional characterization of a cold-active acetyl xylan esterase (PbAcE) from psychrophilic soil microbe *Paenibacillus* sp, PLoS One 13 (2018), doi:<http://dx.doi.org/10.1371/journal.pone.0206260>.
- [73] Understanding Temperature Control in Bioreactor Systems, Thermal Stability in Bioreactors, Process Worldwide, 2021 Accessed 24 April 2020.
- [74] E. Maleki, Psychrophilic anaerobic membrane bioreactor (AnMBR) for treating malting plant wastewater and energy recovery, J. Water Process Eng. 34 (2020) 101174, doi:<http://dx.doi.org/10.1016/j.jwpe.2020.101174>.
- [75] D. Rettori, N. Durán, Production, extraction and purification of violacein: an antibiotic pigment produced by *Chromobacterium violaceum*, World J. Microbiol. Biotechnol. 14 (1998) 685–688, doi:<http://dx.doi.org/10.1023/A:1008809504504>.
- [76] M.T. Sibero, T.U. Bachtiarini, A. Trianto, A.H. Lupita, D.P. Sari, Y. Igarashi, E. Harunari, A.R. Sharma, O.K. Radjasa, A. Sabdono, Characterization of a yellow pigmented coral-associated bacterium exhibiting anti-bacterial activity against multidrug resistant (MDR) organism, Egypt. J. Aquat. Res. 45 (2019) 81–87, doi:<http://dx.doi.org/10.1016/j.ejar.2018.11.007>.
- [77] S. Afra, A. Makhdoumi, M.M. Matin, J. Feizy, A novel red pigment from marine *Arthrobacter* sp. G20 with specific anticancer activity, J. Appl. Microbiol. 123 (2017) 1228–1236, doi:<http://dx.doi.org/10.1111/jam.13576>.
- [78] D. Alem, J.J. Marizcurrena, V. Saravia, D. Davyt, W. Martinez-Lopez, S. Castro-Sowinski, Production and antiproliferative effect of violacein, a purple pigment produced by an Antarctic bacterial isolate, World J. Microbiol. Biotechnol. 36 (2020), doi:<http://dx.doi.org/10.1007/s11274-020-02893-4>.
- [79] S.Y. Choi, S. Kim, S. Lyuck, S.B. Kim, R.J. Mitchell, High-level production of violacein by the newly isolated *Duganella violaceinigra* str. NI28 and its impact on *Staphylococcus aureus*, Sci. Rep. 5 (2015), doi:<http://dx.doi.org/10.1038/srep15598>.
- [80] B. Khanam, R. Chandra, Comparative analysis of prodigiosin isolated from endophyte *Serratia marcescens*, Lett. Appl. Microbiol. 66 (2018) 194–201, doi:<http://dx.doi.org/10.1111/lam.12840>.
- [81] E.N. Grady, J. MacDonald, L. Liu, A. Richman, Z.C. Yuan, Current knowledge and perspectives of *Paenibacillus*: a review, Microb. Cell Fact. 15 (2016) 203, doi:<http://dx.doi.org/10.1186/s12934-016-0603-7>.
- [82] K. Zorn, I. Oroz-Guinea, U.T. Bornscheuer, Strategies for enriching erucic acid from *Crambe abyssinica* oil by improved *Candida antarctica* lipase A variants, Process Biochem. 79 (2019) 65–73, doi:<http://dx.doi.org/10.1016/j.procbio.2018.12.022>.
- [83] P. Maheshwari, I. Kovalchuk, Genetic transformation of crops for oil production, in: T. McKeon, D. Hayes, D. Hildebrand, R. Weselake (Eds.), Industrial Oil Crops, Academic Press, AOCS Press, 2016, pp. 379–412, doi:<http://dx.doi.org/10.1016/B978-1-893997-98-1.00014-2>.
- [84] R. Katna, M. Suhaib, N. Agrawal, Nonedible vegetable oil-based cutting fluids for machining processes—a review, Mater. Manuf. Process. 35 (2020) 1–32, doi:<http://dx.doi.org/10.1080/10426914.2019.1697446>.
- [88] R. Sowmya, N.M. Sachindra, Carotenoid production by *Formosa* sp. KMW, a marine bacteria of Flavobacteriaceae family: Influence of culture conditions and nutrient composition, Biocatal. Agric. Biotechnol. 4 (2015) 559–567, doi:<http://dx.doi.org/10.1016/j.bcab.2015.08.018>.

RESEARCH ARTICLE



WILEY

Sustained release resolvin D1 liposomes are effective in the treatment of osteoarthritis in obese mice

Ameya A. Dravid | Kaamini M. Dhanabalan | Soumyadeep Naskar |
Akshi Vashistha | Smriti Agarwal | Bhagyashree Padhan | Mahima Dewani |
Rachit Agarwal

Indian Institute of Science, Bengaluru, India

Correspondence

Rachit Agarwal, 3rd Floor, Biological Sciences Building, Indian Institute of Science, Bengaluru 560012, Karnataka, India.
Email: rachit@iisc.ac.in

Funding information

Department of Biotechnology, Ministry of Science and Technology, India, Grant/Award Number: BT/12/IYBA/2019/04; Department of Science and Technology, Government of India (SERB Early Career Research Award), Grant/Award Number: ECR/2017/002178; Indian Institute of Science start-up grant

Abstract

Osteoarthritis (OA) is the most common joint disorder and currently affects >500 million patients worldwide, with ~60% of them also suffering from obesity. There is no drug approved for human use that changes the course of OA progression. OA is one of the most common comorbidities of obesity, and obesity-related OA (ObOA) is a serious health concern because it shows heightened severity of tissue damage and also predominantly affects the working population. Unresolved inflammation is a major driver of ObOA, thus, resolving disease-associated inflammation is a viable strategy to treat ObOA. Resolvins are highly potent molecules that play a role in the resolution of inflammation and promote tissue healing. However, small molecules (like Resolvin D1; RvD1) have to be administered frequently or prior to injury because they lose their in vivo activity rapidly either by lymphatic clearance, or oxidation-mediated deactivation. In this study, we have encapsulated RvD1 in liposomes and established its efficacy in the mouse model of ObOA at much lower dosages than freely administered RvD1. Liposomal RvD1 (lipo-RvD1) acted as a source of the RvD1 molecules for ~11 days in vitro in synovial fluid derived from patients. When administered prophylactically or therapeutically, lipo-RvD1 suppressed cartilage damage in male C57BL/6 mice compared to untreated and free RvD1 treatments. This efficacy was achieved by increasing the proportion of the proresolution M2 macrophages over proinflammatory M1 macrophages in the synovial membrane. These results show the potential of lipo-RvD1 as an anti-OA agent.

KEYWORDS

inflammatory diseases, nanocarriers, regenerative medicine, resolution of inflammation, specialized pro-resolution mediators

1 | INTRODUCTION

Osteoarthritis (OA) is a highly prevalent disease of the articulating joints. Recent reports show that >500 million patients worldwide are affected by OA.¹ OA is known to progressively degrade cartilage and the subchondral bone. Obesity is also heavily linked with OA, where ~59% of all OA patients are also obese.² Obesity actively contributes to the progressing

cartilage damage via excessive joint loading and elevated inflammatory signaling to subsequently produce an accelerated pathology.³ Current treatment for OA focuses only on palliative care by administration of analgesics without improving joint function.⁴ Steroidal analgesics have several drawbacks like chronic chondrotoxicity and cartilage thinning and are not recommended for long-term administration.⁵ Obesity is also characterized by systemic dyslipidemia and the generation of hypertrophic adipocytes

and fat depots, which dysregulate the release of several adipokines like resistin, leptin, and visfatin,⁶ of which impairment of leptin-mediated signaling is a major contributor to OA.⁷ Such impaired adipokine-mediated signaling triggers the release of proinflammatory cytokines like IL-1 β and TNF- α in both the systemic circulation and the synovium.^{7,8} Hence, obesity-related metabolic dysregulation contributes to the prevailing chronic OA-associated inflammation and increases tissue damage,⁶ and targeting this inflammation is hence a viable strategy to treat ObOA.

Previous attempts that delivered anti-inflammatory molecules to the site of damage have not succeeded in translating into therapy for humans^{9,10} despite the encouraging results in small animal models.^{11,12} Synovial vasculature rapidly clears small molecules, while the lymphatics drain away macromolecules,^{13,14} resulting in short half-lives in the joint (1–4 h) for commonly used steroids.^{4,15} Such molecules, when encapsulated in particles, show increased intraarticular retention because the relatively larger size of the particles prevents lymphatic drainage-mediated clearance.¹⁶ One of the preferred particle-based drug carriers are liposomes. One such liposomal formulation containing palmitoylated dexamethasone, Lipotalon[®], has been approved in Germany for treating OA-related pain in patients. Liposomal carriers have demonstrated favorable properties like low toxicity, biodegradability, stability, flexible synthesis methods, and ability to incorporate cargo with diverse properties (imaging agents, corticosteroids, MMP inhibitors)^{17–19} and are hence ideal carriers of drugs. These particles have been used for the intraarticular delivery of corticosteroids,^{20,21} and can be used for immunomodulation in OA as well.²² Liposome-encapsulated molecules show a \sim 10-fold increase in intraarticular (IA) retention than molecules injected directly.¹⁶ Liposomes have a predictable release of the loaded drugs into the extraliposomal space, thus helping in the process of dosing in humans.¹⁶

Specialized proresolution mediators (SPMs)²³ are potent molecules that actively reduce inflammatory factors from the site of damage^{23–25} in a process called resolution of inflammation. Chronic inflammatory diseases, including ObOA, are known to have impaired inflammation resolution pathways.^{26,27} Exogenously supplied SPMs like RvD1 reduce the severity of OA, but strategies involving the direct intraarticular injection of such molecules require high doses and administration of doses before OA-causing injury has taken place.²⁸ Our previous efforts have demonstrated the improved anti-OA efficacy of liposomal RvD1 compared to free RvD1 in a chow-fed mouse model of PTOA.¹⁶ Hence, we wanted to test our formulations in a more clinically relevant and challenging model of ObOA.

In this study, we show that in a mouse model of ObOA, liposome-based delivery of RvD1 significantly improved joint health than untreated and free RvD1 delivery. Our mechanistic analysis shows that this protective action is mediated via the action of the released RvD1 on cells like macrophages in the synovium.

2 | METHODS

2.1 | Materials

The lipids dipalmitoylphosphatidylcholine (DPPC), 1, 2-Distearoyl-sn-glycero-3-phosphoethanolamine-Poly (ethylene glycol) (DSPE: PEG),

Cholesterol, Dioleoyl-3-trimethylammonium propane (DOTAP) were purchased from Avanti polar lipids. Resolvin D1 was purchased from Cayman chemicals. Syringes were purchased from BD Biosciences. Antibodies used: anti-iNOS (NB300-605) and anti-CD206 (NBP1-90020) antibodies were purchased from Novus biological (Centennial, Colorado, United States). Anti-ADAMTS5 (ab41037) and anti-MMP13 (ab39012) antibodies were purchased from Abcam (Cambridge, United Kingdom). An anti- β -catenin antibody was purchased from ThermoFisher Scientific (71-2700). Solvents: acetonitrile, methanol, and HPLC grade water were purchased from Fisher Chemicals. All purchased compounds were used without further purification.

2.2 | Synthesis and characterization of liposomes

Liposomes were synthesized by the thin-film lipid hydration method. Briefly, the lipids DPPC, DSPE-PEG, and cholesterol were dissolved in chloroform and mixed in their respective molar ratios in a round bottom flask. The chloroform was evaporated using a rotatory evaporator (DLAB RE100 Pro), thus forming thin lipids films. The films generated were hydrated using respective solutions (AF750 in phosphate buffered saline [PBS] for in vivo retention experiments, calcium acetate for all RvD1 loading experiments) at 45°C. The vesicles were then collected and passed through 1 μ m and 400 nm membranes to generate liposomes of a defined size. The sizes of liposomes were measured using Malvern Zetasizer μ V.

2.3 | Cryogenic transmission electron microscopy of liposomes

Liposomes were imaged using a cryogenic transmission electron microscope (Cryo-TEM). Briefly, Holey Carbon Flat R2/2 grids were blotted with a liposomal solution (2 mg/mL) and plunged into liquid ethane using FEI vitrobot to generate vitrified samples. These samples were stored in liquid nitrogen till further use. Furthermore, images of these samples were captured using Thermo Scientific Arctica equipped with a Gatan K2 direct electron detector camera by Latitude S software with a spot size of 7. The total exposure was 40 e⁻/Å², and the pixel size was 1.2 Å.

2.4 | Loading of RvD1 into liposomes

RvD1 was loaded into liposomal using a remote-loading strategy as mentioned earlier.¹⁶ Briefly, thin films of lipids were hydrated with 120 mM Calcium acetate (pH = 6) to generate multilamellar vesicles. These vesicles were extruded through filters of different pore sizes (1 μ m and 400 nm) to generate liposomes of desired sizes. Finally, the liposomes were pelleted and resuspended in RvD1-containing sodium sulfate solution (pH = 4) and loaded at 50°C for 1.5 h. The loading levels were adjusted to 50 ng RvD1/mg of lipids. After loading, the formulation was washed twice in PBS and used immediately.

2.5 | Release profiles

For characterizing the retention of RvD1, liposomes were incubated in 50% synovial fluid obtained from joints of OA patients (IHEC approval number MSRMC/EC/AP-06/01-2021 at Ramaiah Medical College, Bangalore and 02/31.03.2020 at Indian Institute of Science, Bangalore) for up to 11 days at 37°C. At each time point, the liposomes were washed and lyophilized. Lyophilized powder was dissolved in 50% isopropanol and the samples were loaded and quantified using HPLC as described elsewhere.¹⁶

2.6 | Mice for in vivo studies

The in vivo studies were approved by the Institutional Animal Ethics Committee (CAF/Ethics/808/2020). Male C57BL/6 mice (aged 6–8 weeks; weight 20–22 g) were used for this study, maintained in individually ventilated cages at the central animal facility (CAF), Indian Institute of Science, Bangalore. Depending upon the group, the mice had ad libitum access to either a specialized diet enriched in fat (to model obesity by feeding diet prepared by the National Institute of Nutrition [India] according to Research Diets formulation 12492) or chow (control diet). A cocktail of Ketamine (60 mg/kg) and Xylazine (9 mg/kg) was used to anesthetize animals during procedures.

2.7 | Mice model of ObOA

The surgery for modeling ObOA, destabilization of the medial meniscus (DMM),^{28–30} was performed in mice after 8 weeks of high-fat feeding, as mentioned earlier. The experiments utilized male mice because surgery-induced-OA show more dramatic effects on the cartilage of male mice than that of female mice.³¹ One knee joint was subjected to this surgery in each mouse. On the day of the surgery (after completion of 8 weeks of high-fat feeding), the mice were anesthetized using a cocktail of Ketamine (60 mg/kg) and Xylazine (9 mg/kg). After confirming the loss of pedal reflexes, a parapatellar skin incision was made to access the synovium. The synovium was then dissected to expose the underlying joint. The medial meniscotibial ligament (MMTL) was located and surgically transected. After confirming the successful transection of the MMTL by another observer, the synovium and skin were sutured in layers, and a metronidazole wet pack was applied over the sutured area. The mice were then allowed to recover from the anesthesia on a lukewarm surface. Post-operative analgesic care included four subcutaneous doses of Buprenorphine (0.1 mg/kg), once every 12 h. Later, the mice were administered their respective intraarticular treatments over the next 3 months, as indicated in the result section. The mice were allowed to move freely for the entire duration of the study. During the entire postoperative period, the mice were allowed access to high-fat feed. At the end of the study, the mice were euthanized, and their knee joints were harvested. The joints were fixed in 4% formaldehyde for

6 h and decalcified in 5% formic acid for 5 days. Following decalcification, the joints were dehydrated in multiple gradients of ethanol and xylene and finally embedded in paraffin wax.

2.8 | Quantification of serum parameters

Blood was collected from mice using retroorbital venipuncture. Blood was then allowed to clot at room temperature for 2 h, following which the collection tubes were centrifuged (8000 g, 10 min, 4°C). In this process, the clotted blood forms a pellet at the bottom of the tube, while the liquid fraction (serum) of the blood is at the top. From these tubes, the supernatants were collected and used for further analysis. Analysis kits for total cholesterol, LDL-cholesterol, and total triglycerides were quantified using colorimetric kits from Delta Lab (Maharashtra, India) as per the manufacturer's instructions.

2.9 | Histology and staining

The tissues embedded in paraffin blocks were sectioned into 5 µm thick sections using Leica HistoCore MULTICUT and collected on poly-L-lysine-coated glass slides. The sections were hydrated using a series of ethanol gradients and stained using the Safranin-O.³² The severity of the disease was quantified on a scale of 0–24 using a scoring protocol prescribed by OARSI.³³ This protocol considers the joint's damage, including loss of proteoglycan, chondrocyte apoptosis, and the presence of osteophytes.³³ In this study, the medial surfaces were used for analysis because lateral surfaces did not show significant damage (Figure S1). Scoring was done by trained veterinarians blinded to the study.

2.10 | Measurement of synovial thickness

To quantify fibrosis, we measured the thickness of the synovial membrane (SM). Briefly, joint sections were stained with the Safranin-O staining technique (as mentioned earlier) and images of the respective SMs were captured. The thicknesses of the SMs covering the medial regions of the joints were then measured at three different locations along their lengths using ImageJ.

2.11 | Quantification of cells in the SM

We quantified the severity of synovitis by measuring cellular density in the SM. Briefly, joint sections were stained with the Safranin-O staining technique (as mentioned earlier) and images of the respective SMs (~3 images from each SM) were captured. The number of cells was counted using specialized macros implemented in ImageJ. This number was normalized to the area of the tissue used to quantify the number of cells.

2.12 | Immunohistochemistry

IHC was performed to quantify iNOS⁺ cells, CD206⁺ cells, MMP13⁺, and ADAMTS5⁺ regions in the synovium and cartilage. This method of IHC was derived from our previous studies where several other markers like iNOS, CD206, and LC3B were used for cellular analysis.^{16,34} Briefly, heat-induced epitope retrieval was performed using Tris-EDTA overnight treatment at 65°C, followed by retrieval with 1 N HCl and Trypsin-CaCl₂ (0.05% Trypsin in 1×PBS and 1% CaCl₂). The resulting sections were then incubated with primary antibody (concentrations of antibodies used: anti-iNOS—1 µg/mL; anti-CD206—0.66 µg/mL; anti-MMP13—1 µg/mL; anti-ADAMTS5—0.33 µg/mL) for 16 h. These sections were then washed to remove excess unbound antibody and incubated with horseradish peroxidase (HRP)-conjugated secondary antibody (1.6 µg/mL) for 2 h. After washing the unbound secondary antibody, sections were incubated with 3,3'-diaminobenzidine (DAB) substrate for 1 h. Excess unreacted DAB was washed, and images were captured using an Olympus BX53F brightfield microscope. The images were thresholded against the background and counted using the “analyze particles” module in ImageJ.

2.13 | Testing for mechanical allodynia

OA-associated allodynia was tested using von Frey filaments (Aesthesio tactile sensory filament, Ugo Basile). Briefly, the animals were introduced in a customized cage with perforated bottom and were allowed to be acclimated to it for a few minutes. A von Frey filament representing the smallest force was pushed against the plantar regions of the paw of respective animals through the perforations in the cage. This exercise was performed 10 times per filament. If the animal withdrew its paw three out of 10 times, the force represented by that filament was noted as the paw withdrawal threshold. If no such activity was seen, the exercise was continued with the next filament. Only animals with no visible injury were used for data collection.

2.14 | Statistics

Data presented in this manuscript were represented as mean ± SD with at least three replicates in each group unless stated otherwise. Data were analyzed using one-way analysis of variance for normal distributions and using other non-parametric tests (e.g., Dunn's or Kruskal-Wallis tests) for ordinal datasets. Outliers were analyzed using the Grubbs test ($\alpha = .05$). If an outlier was detected in any assay, then the data from that animal was completely excluded from all other assays. The 95% confidence interval was considered significant. Power analysis (power = 0.8, $\alpha = .05$) yielded the desired sample size of 8–11 mice per group.

3 | RESULTS

3.1 | Lipo-RvD1 creates a depot of RvD1 in human synovial fluid

Liposomes were synthesized using the thin film hydration followed by extrusion through 400 nm pore size membranes as described earlier.¹⁶ The size and zeta potential was found to be 312 ± 10.1 nm and -1.92 ± 0.05 mV respectively (Figure 1A,B). Synthesis was followed by loading of RvD1 into liposomes using an active encapsulation strategy (E.E. = $55.6 \pm 24.5\%$). To evaluate the sustained release of RvD1 from the formulation in the synovium-like conditions, lipo-RvD1 was incubated in synovial fluid (obtained from patients undergoing joint replacement surgery) at 37°C for various time intervals. At each of these intervals, liposomes were collected and the drug retained was quantified using HPLC. HPLC quantification showed that RvD1 molecules were retained intraliposomally for ~11 days (Figure S2).

3.2 | Obesity can be induced in mice by high-fat feeding

Obesity is characterized by an increase in body weight due to the deposition of excessive fat in adipose tissue.³⁵ This disorder can be modeled in mice by providing ad libitum access to specialized diets which are enriched in fat.^{36,37} In our experiments, we used a specialized feed containing 60% fat by calorie content to generate overweight mice. We observed a statistically significant difference between the weights of the chow-fed and HFD-fed mice from the 8th week after the commencement of feeding (Figure 1C). Obese patients often show systemic dyslipidemia and upregulated low-density lipoprotein fraction of cholesterol (LDL-c), triglycerides, and cholesterol.^{38,39} Accordingly, we found that the total cholesterol (TC) was higher in the serum of overweight mice than in their leaner counterparts (Figure 1D). LDL-c also increased with dietary fat in mice (Figure 1D) and the ratio of both TC (Figure 1F) and LDL-c (Figure 1G) to the high-density lipoprotein fraction of cholesterol (HDL-c) was higher in overweight mice than in their leaner counterparts. Since these parameters were in alignment with those reported in the literature,⁴⁰ high fat-fed mice were successfully classified as obese.

The destabilization of the medial meniscus (DMM) is a widely used surgical model for obesity-related post-traumatic OA (PTOA).^{28,30} The medial meniscus, located between articulating surfaces, provides stability to the joint by absorbing mechanical shock. Surgically cutting and dislocating this tissue mimics damage resulting from traumatic events like sports injuries and accidents and results in contact between the two articulating surfaces. This surgery generates OA-like changes over 1–3 months. To mimic ObOA, we performed DMM in obese mice and compared it with DMM in mice fed with standard diet (11% kCal by fat). We found more severe damage to the cartilage in obese mice than in their leaner counterparts after DMM surgery ($p = .032$) (Figure 1H,I). Furthermore, we observed that obesity alone was not sufficient to increase the severity of OA, as seen from the comparison between the pathologies of lean and obese sham joints (Figure 1H,I). We also showed that the articulating

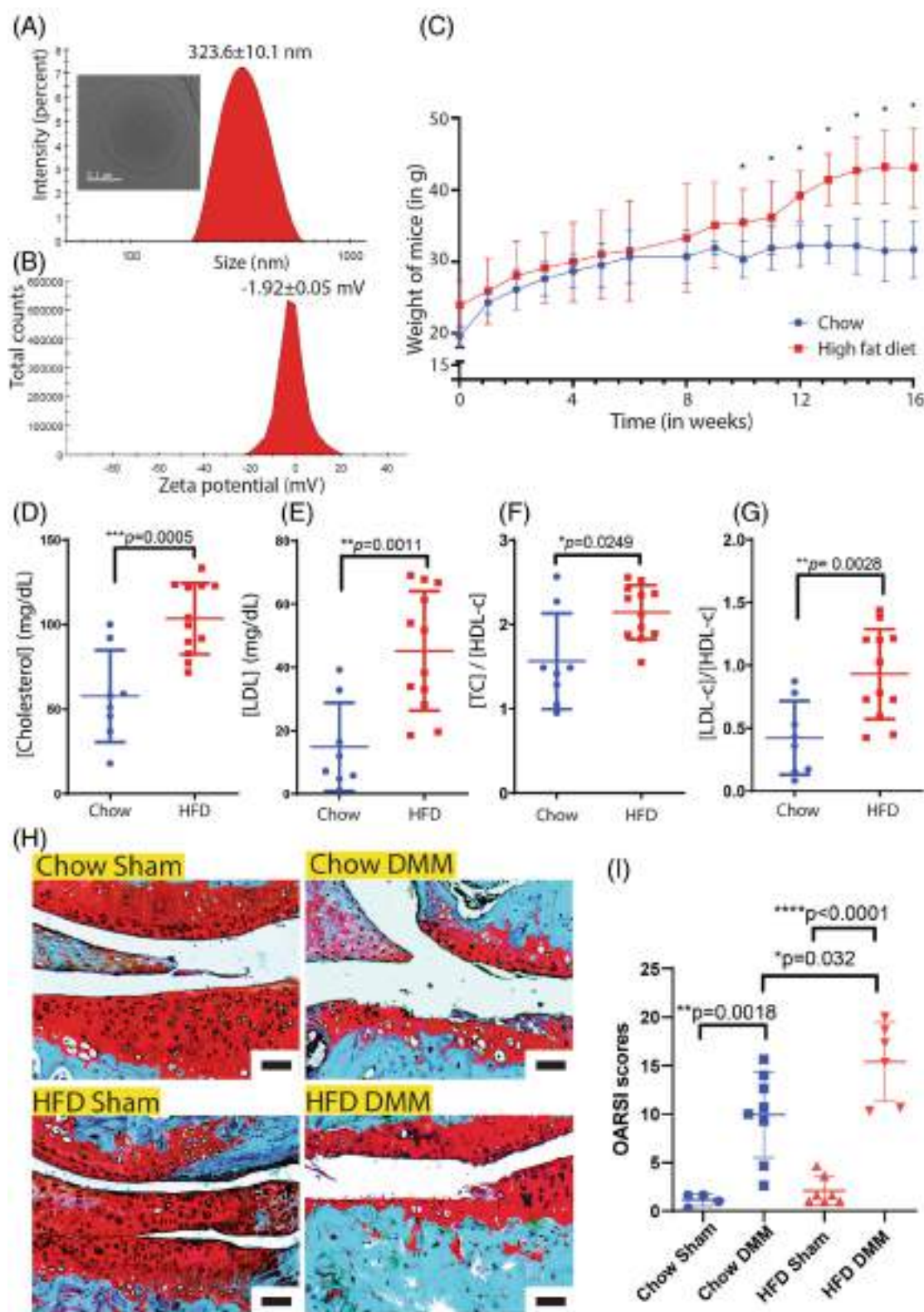


FIGURE 1 High-fat fed mice become obese and show severe cartilage damage after destabilization of the medial meniscus (DMM) surgery. (A) Size estimation of liposomes using DLS and cryoTEM (inset). (B) Surface charge of liposomes as indicated using zeta potential. (C) Body weight profiles of mice fed high-fat diet (HFD) and chow. Serum levels of (D) cholesterol, (E) LDL, and the serum ratios (F) TC/HDL-c and (G) LDL-c/HDL-c; $n = 8$ lean animals and $n = 12$ obese animals. (H) Characteristic Safranin-O stained sections of cartilage (scale bar 50 μ m). (I) OARSI scores indicating the severity of the joint damage; $n = 4$ –8 animals per group. For D, E, F, G, and I, $*p < .05$; $**p < .01$; $***p < .001$; and $****p < .0001$ between the respective groups indicated in the figures using analysis of variance (ANOVA) followed by Tukey's posthoc test. For C, $**p < .01$ between the respective groups indicated in the figures using multiple t tests. Values are expressed as mean \pm SD. Scale bar 50 μ m.

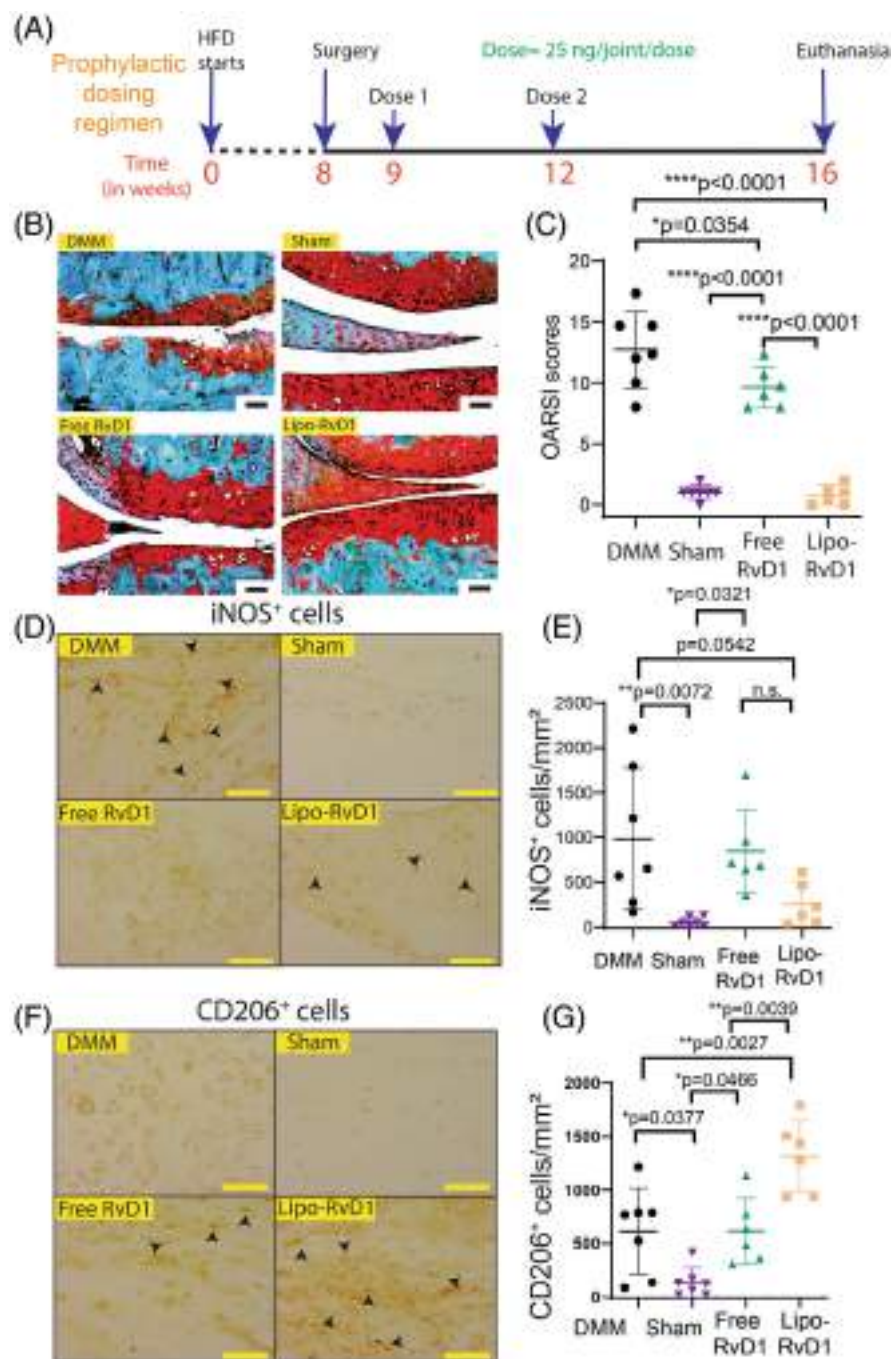


FIGURE 2 Prophylactic administration of lipo-RvD1 maintains cartilage integrity. (A) Timeline of the experiment. (B) Characteristic Safranin-O-stained histology sections of different groups of mice (scale bar 200 μ m). (C) OARSI scores of Safranin O-stained sections of mice knee joints administered with respective treatment; $n = 7-8$ animals per group. (D) IHC images depicting levels of iNOS+ M1 macrophages synovial membrane (scale bar 50 μ m). (E) Quantification of iNOS+ M1 macrophages in the synovial membrane; $n = 7-8$ animals per group. (F) IHC images depicting levels of CD206+ M2 macrophages in synovial membrane (scale bar 50 μ m). (G) Quantification of CD206+ M2 macrophages in the synovial membrane; $n = 7-8$ animals per group. For C, E, and G two points in the free RvD1 and two in lipo-RvD1 group were removed after outlier analysis (Grubbs test). For C, E, and G $*p < .05$; $**p < .01$; and $***p < .0001$ between the respective groups indicated in the figures using analysis of variance (ANOVA) followed by Tukey's posthoc test. Values are expressed as mean \pm SD. Scale bar 50 μ m.

surfaces in both the chow-fed DMM and high-fat diet DMM were severely denuded, with more damage expressed in the latter (damage in obese mice is $\sim 1.5\times$ more severe compared to their leaner counterparts). This finding is in agreement with earlier studies which showed that obesity is the major contributor to the pathology.⁷

3.3 | Lipo-RvD1 is a good prophylactic candidate for ObOA treatment

We performed DMM surgery in obese mice and used a prophylactic dosing regimen by injecting freshly synthesized lipo-RvD1

intraarticularly (IA) at weeks 1 and 4 after surgery (Figure 2A). Lipo-RvD1 arrested the progressing cartilage damage and maintained the overall joint integrity. In the case of lipo-RvD1-treated mice, the OARSI scores were similar to sham mice. There was a 6–8-fold reduction in OARSI scores of lipo-RvD1 treated mice compared to DMM joints ($p < .0001$), which had complete loss of articulating cartilage at certain sites of damage (Figure 2B,C). IA injection of blank liposomes failed to show any efficacy (Figure S3). Figure 2B,C also depict that more chondrocytes were observed to be healthy in the lipo-RvD1 treated joint than in free RvD1 and DMM joints. Administration of free RvD1 also showed some protective effect on the joint but the OARSI scores were still significantly higher than sham group

($p < .0001$). Several inflammatory diseases have an imbalance between the M1 and M2 macrophages.^{30,41,42} The ratio of M1/M2 cells is skewed in OA as well and proinflammatory cytokines from M1 macrophages drive cartilage damage.⁴³ Previously it was shown that prophylactically administered RvD1 improves the ratio of M1/M2 macrophages in the SM.^{16,28} As seen from our results, DMM mice had higher levels of iNOS⁺ M1 cells than sham mice, which indicates the presence of a proinflammatory environment in the synovium ($p = .0072$) (Figure 2D,E). Furthermore, lipo-RvD1 treatment promoted polarization toward M2 cells as compared to all other groups, evident by an increased number of CD206⁺ cells (Figure 2F,G). Overall, we observed that lipo-RvD1 formulation was increasing M2 macrophages in the joint which reduced the net inflammatory activity within the synovium and promoted clearance of debris and other inflammatory factors. This inference, however, could not be extrapolated to other regions of the joint (Figure S4). In OA, chondrocytes release catabolic enzymes like ADAMTS5 and MMP13, which also are recognized as markers of chondrocyte hypertrophy.⁴⁴ Administration of lipo-RvD1 suppressed the expression of the catabolic mediators MMP13 (but not ADAMTS5), thus preventing the formation of hypertrophic chondrocytes in mice (Figure S5).

3.4 | Lipo-RvD1 is effective as therapeutic treatment in ObOA

In clinics, the diagnosis of OA relies on radiographic evidence of joint damage, which is visible only when the damage has progressed significantly.⁴⁵ Accordingly, therapeutic formulations are critical for the successful treatment of OA. Hence, we tested the therapeutic efficacy of lipo-RvD1 by injecting it at 3 and 6 weeks after DMM surgery. This timeline was chosen as a suitable therapeutic regimen because cartilage damage is known to start within 2 weeks after DMM⁴⁶ (Figure 3A). In this challenging regimen, IA-administered lipo-RvD1 significantly reduced OARS scores compared to free RvD1-administered joints ($p = .0006$) and DMM-only joints ($p = .0001$) (Figure 3B,C). M1 macrophages were present in large numbers in the SM of the DMM-treated joints compared to the lipo-RvD1-treated joints, but the difference was not statistically significant (Figure 3D,E). However, the therapeutic regimen of administration of lipo-RvD1 showed increased levels of pro-resolution M2 macrophages compared to DMM ($p = .0002$) or free RvD1 ($p = .0006$) (Figure 3F,G). We further observed that the lipo-RvD1 treatment reduced the expression of damaging enzymes like MMP13 and ADAMTS5 compared to free-RvD1 treatment and protected cartilage from degradation (Figure S6). To evaluate the minimum required doses of lipo-RvD1 to achieve anti-OA efficacy, we further reduced and administered one dose (given at 12 weeks) over the total experiment (Figure S7A). Our OARS scores and histology results showed that this regimen was not sufficient to protect the joint from impending OA-related joint damage (Figure S7B,C). However, it is possible that administration of lipo-RvD1 can improve

efficacy if given at an earlier time point which was not explored in this study.

Wnt signaling plays a major role in OA pathology⁴⁷ and inhibitors of this pathway (e.g., lorecivint-phase 3 clinical trials; NCT04931667) are currently in clinical trials as an anti-OA medication.⁴⁸ β -catenin is a mediator of Wnt signaling and is upregulated in OA.⁴⁷ In our prophylactic study, we observed that both free RvD1 and lipo-RvD1 administration to OA joints suppressed the overexpression of β -catenin in chondrocytes (Figure S8A), thus indicating the ability of RvD1 to regulate Wnt signaling. Furthermore, in our therapeutic study, we observed that administration of free RvD1 was not sufficient to prevent overexpression of β -catenin, and this regulation of Wnt signaling was achieved only if RvD1 was administered in a sustained manner through liposome-encapsulated RvD1 (Figure S8B). It is not clear how RvD1 administration is modulating Wnt signaling and more experiments are required to understand this phenomenon.

One of the hallmarks of advanced OA is the development of chondrocytes, which develop into osteophytes. These characteristics are also observed in the DMM model for OA.¹⁶ In our studies, although some of the joints demonstrated these features, a majority of them were devoid of chondrocytes (Figure S9).

3.5 | Lipo-RvD1 reduces synovitis in mice

Synovitis is a hallmark of OA⁴⁹ and is characterized by an increased pool of leukocytes in the SM. Synovitis increases the production of inflammatory mediators which leads to chondrocyte hypertrophy and blocks anabolism.⁵⁰ Our data showed that treating DMM mice with lipo-RvD1 reduced the SM thickness (Figure 4A–D) and cellularity (Figure 4E–H) as compared to DMM-only mice, in both, therapeutic and prophylactic regimens of administration. SM from lipo-RvD1-treated joints was similar in thickness to SM in sham joints in both the therapeutic and prophylactic regimens of administration, thus emphasizing the ability of lipo-RvD1 to suppress excessive fibrosis of SM (Figure 4A–D). We observed that in the therapeutic regimen, lipo-RvD1 treated membranes were thinner than free RvD1 treated membranes ($p = .0118$). This result also held true for the total cellularity of the SM (Figure 4E–H). Lipo-RvD1 treated joints showed a better ability to prevent cells from infiltrating the inflammatory milieu compared to free RvD1 when administered therapeutically ($p = .0002$) (Figure 4G,H).

3.6 | Lipo-RvD1 reduces the incidence of OA-associated allodynia

OA patients suffer from pathological pain (allodynia).⁵¹ Pain threshold was tested using Von Frey filaments 8 weeks after surgery (immediately before euthanasia). We observed that administration of lipo-RvD1 was more effective in alleviating the allodynia than free RvD1 injected mice ($p = .0009$) in the prophylactic regimen of administration (Figure 5A) but not in the therapeutic regimen

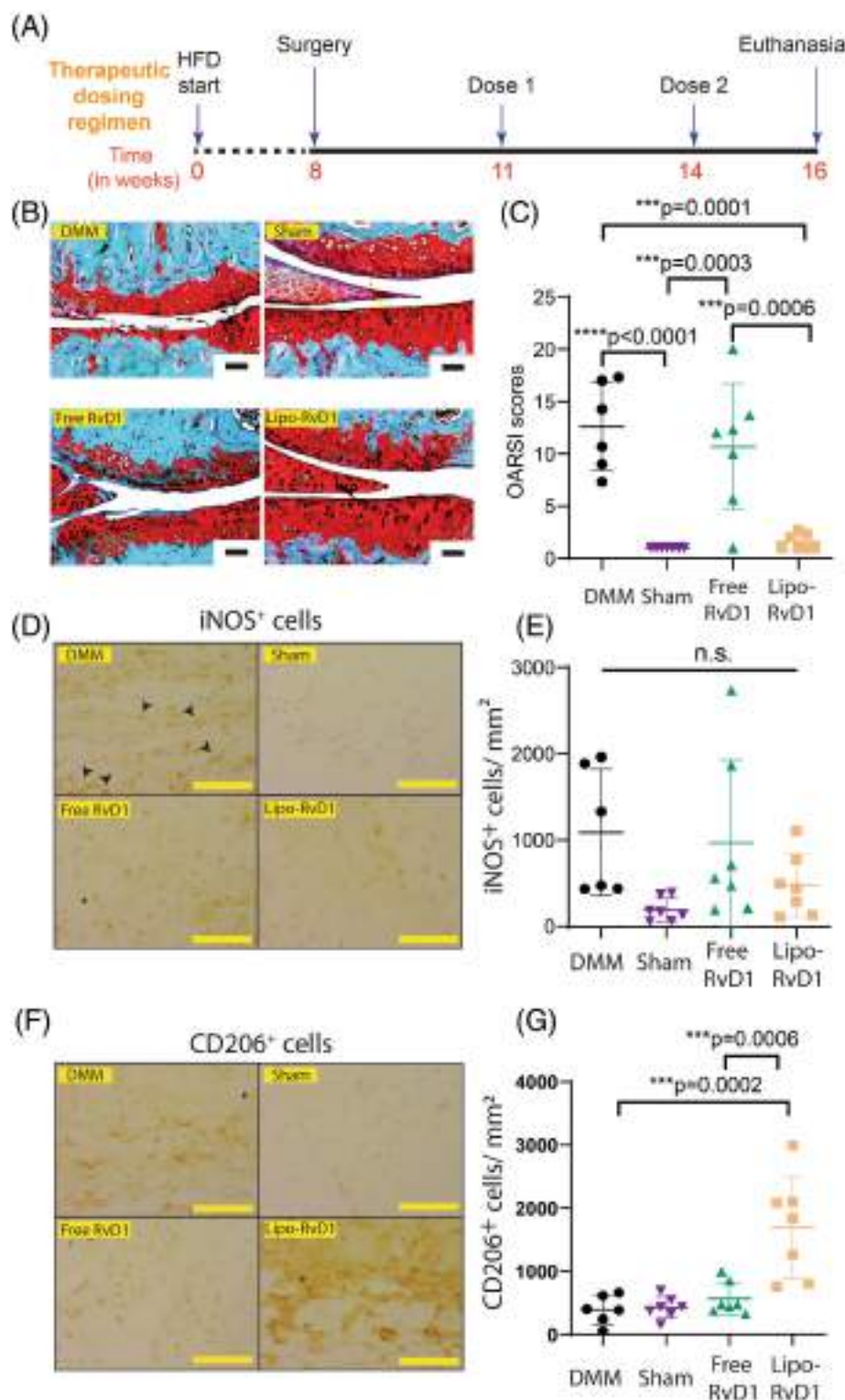


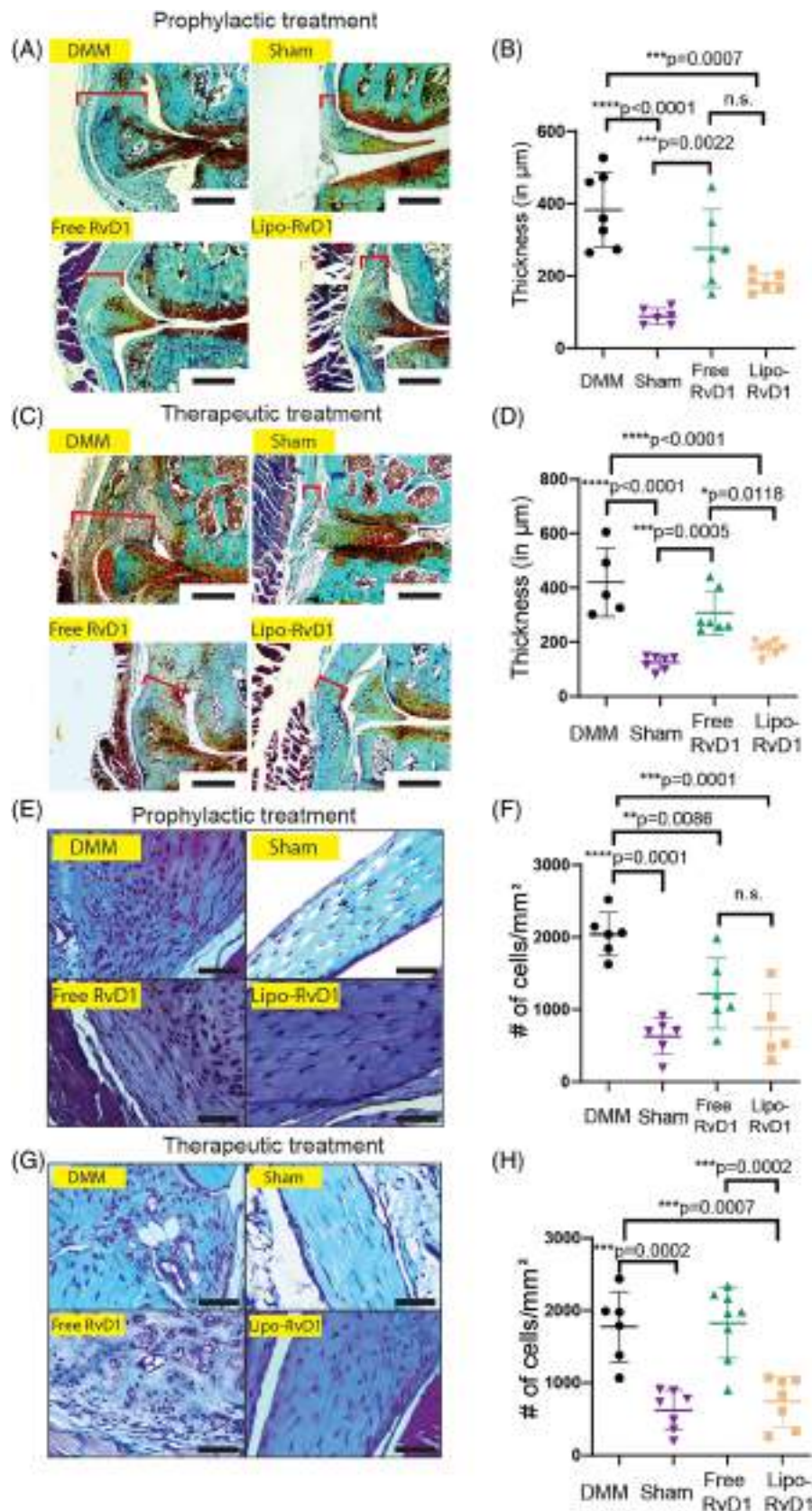
FIGURE 3 Therapeutic administration of lipo-RvD1 protects cartilage from progressing damage. (A) Timeline for the study. (B) Safranin-O-stained characteristic histological images of different groups of animals (scale bar 200 μ m). (C) OARSI scores of Safranin-O-stained sections of mice joints administered with respective treatment; $n = 6-8$ animals per group. (D) Characteristic IHC images depicting levels of iNOS⁺ M1 macrophages in the synovial membrane of respective mice joints (scale bar 50 μ m). (E) Quantification of iNOS⁺ M1 macrophages in the synovial membrane of respective mice joints; $n = 6-8$ animals per group. (F) IHC images depicting levels of CD206⁺ M2 macrophages in synovial membrane (scale bar 50 μ m). (G) Quantification of CD206⁺ M2 macrophages in the synovial membrane; $n = 6-8$ animals per group. For C, E, and G, $***p < .001$ and $****p < .0001$ between the respective groups indicated in the figures using analysis of variance (ANOVA) followed by Tukey's posthoc test. n.s., non-significant. Values are expressed as mean \pm SD. Scale bar 50 μ m.

(Figure 5B). IA administration of free RvD1 did not generate adequate analgesia in the therapeutic regimen, and the paw-withdrawal threshold of these mice was not statistically different than that of DMM-operated mice (Figure 5B). Our results from the therapeutic regimen showed that lipo-RvD1 improves the pain threshold of the limb, but the difference was not statistically significant compared to free RvD1 (Figure 5B).

4 | DISCUSSION

Obesity is one of the most common sources of metabolic dysfunction in humans and contributes to the pathology of several diseases by mediating metabolic dysregulation, including OA.^{3,52} In obesity, the adipose tissue is affected, which acts as an endocrine organ to release several proinflammatory adipokines and cytokines like leptin⁶ and

FIGURE 4 Lipo-RvD1 treated mice show reduced synovitis. (A) Images of stained sections of synovial membranes of joints treated with lipo-RvD1 prophylactically. (B) Thickness of the synovial membrane of joints treated with lipo-RvD1 prophylactically; $n = 6-8$ animals per group. (C) Images of stained sections of synovial membranes of joints treated with lipo-RvD1 therapeutically. (D) Thickness of the synovial membrane of joints treated with lipo-RvD1 therapeutically; $n = 5-8$ animals per group. (E) Magnified images of stained sections of synovial membranes of joints treated with lipo-RvD1 prophylactically. (F) Quantification of cells in the synovial membrane of joints treated with lipo-RvD1 prophylactically; $n = 6-8$ animals per group. (G) Magnified images of stained sections of synovial membranes of joints treated with lipo-RvD1 therapeutically. (H) Quantification of cells in the synovial membrane of joints treated with lipo-RvD1 therapeutically; $n = 6-8$ animals per group. For B, D, F, H, * $p < .05$; ** $p < .01$; *** $p < .0001$; and **** $p < .0001$ between the respective groups indicated in the figures using analysis of variance (ANOVA) followed by Tukey's posthoc test. n.s., non-significant. Values are expressed as mean \pm SD. Scale bar 50 μm .



IL-6.⁸ The ratio of ω -3 to ω -6 fatty acids is also skewed in the adipose tissue.⁵³ Studies have shown that RvD1 is downregulated in obese tissue.⁵⁴ Improving this ratio by increasing the dietary ω -3 fatty acids is

known to improve the inflammatory tone of the tissue^{55,56} (this phenomenon is also observed in OA^{57,58}). Reports also suggest that RvD1 (an ω -3 fatty acid) reduces the levels of leptin in adipocytes in vitro,⁵⁹

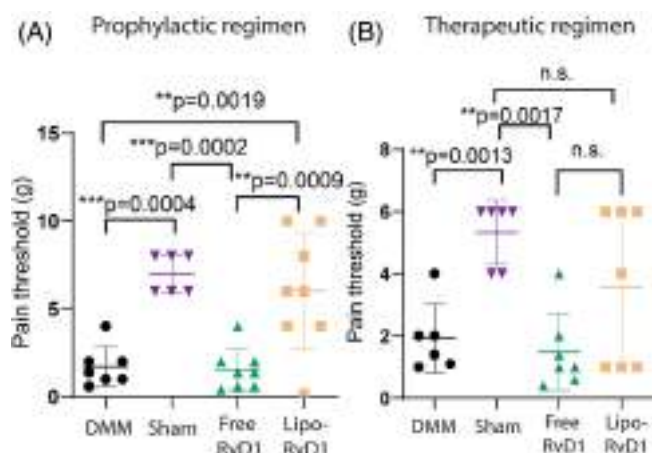


FIGURE 5 Lipo-RvD1 shows analgesia in prophylactic but not in the therapeutic regimen. Paw withdrawal thresholds were obtained using von Frey filaments in mice administered lipo-RvD1 (A) prophylactically and (B) therapeutically; $n = 6-8$ mice per group in both studies. For A and B, $**p < .01$; $***p < .001$; and $****p < .0001$ between the respective groups indicated in the figures using analysis of variance (ANOVA) followed by Tukey's posthoc test. n.s., non-significant. Values are expressed as mean \pm SD. Scale bar 50 μ m.

thus promoting healthy adipose tissue. We had previously shown that administration of lipo-RvD1 was efficacious in chow-fed mice.¹⁶ All these studies motivated us to explore the effect of RvD1 in the treatment of OA in obese mice.

Macrophages are immune cells with significant plasticity which allows them to perform diverse roles like wound healing, tissue homeostasis, and protection against inflammation.⁶⁰ Traditionally, the entire spectrum of macrophages could be divided into two broad phenotypes-M1 phenotype, which is responsible majorly for a proinflammatory response, and M2 macrophages, which are dominant in a proresolution medium.⁶⁰ These phenotypes are dynamic and can change depending on the factors present in the surrounding. In the case of several inflammatory diseases, chronically activated proinflammatory M1 macrophages are the major aggressors of tissue damage, and increasing the fraction of M2 macrophages is a viable strategy for the treatment of such diseases.^{28,60} We observed that administration of lipo-RvD1 improves the levels of M2 macrophages while simultaneously suppressing the M1 phenotype compared to DMM joints. Furthermore, for the dose of RvD1 that we administered (25 ng/joint), this phenomenon was observed only when the molecule was administered in a liposome-encapsulated, controlled-release format. We did not observe a significant reduction of M1 macrophages in the SM of lipo-RvD1 treated joints compared to free-RvD1. In this study, we used iNOS and CD206 as markers for M1 and M2 macrophages respectively. While these markers are well-accepted,^{28,61} endothelial cells and other immune cells also express CD206 and iNOS respectively. Other markers of macrophages and its subtypes can further increase confidence in data.

Liposomes have several advantages like biocompatibility, flexible synthesis, and stability for a long duration. For these reasons, liposomes are the most commonly approved sustained-release formulations for

human use. In our previous study, we also reported that liposome-mediated delivery of drugs improved their IA retention compared to free molecules.¹⁶

Pathological neuropathic pain is a major consequence of OA, and has two common symptoms: allodynia (pain due to stimuli that is not normally painful) and hyperalgesia (increased sensitivity to painful stimuli).⁶² The nature of pain depends on the nature of the stimuli generating the pain.⁶² This study evaluates allodynia (pain generated from von Frey filaments that are normally considered painless), but does not investigate the hyperalgesic behavior of mice in the respective group. This limitation prevents us from gaining a broad perspective on the analgesic properties of Lipo-RvD1 and will be addressed in future experiments.

The transient receptor potential (TRP) family of mediators is critical in the response to mechanical stimuli, including those inducing pain.⁶³ In OA, members of this family of receptors, especially TRPV1 and TRPV4, are associated with the severity of pain.⁶⁴⁻⁶⁶ RvD1 has been shown to generate analgesia in different models by targeting a few members of this family, like TRPV3, TRPV4, and TRPA1.^{67,68} RvD1 receptors are also known to play a role in analgesia.⁶⁹ Our results show that the sustained presence of RvD1 in the affected knee joint helps alleviate OA-associated pain, especially under a prophylactic regimen. The ability of lipo-RvD1 to provide analgesia can ensure higher patient compliance and also improve the translational and clinical relevance of the formulation. Several other mechanisms of pain have been discovered, including the role of mechanotransducers like PIEZO.⁷⁰ However, no direct interaction between RvD1 and these receptors have been discovered, and hence their role in the proresolution activity of RvD1 remains elusive.

One of our interesting findings includes the ability of lipo-RvD1 to provide analgesia in prophylaxis, but not when administered as a therapeutic agent. In OA (both, human OA⁷¹ and collagen-induced mouse models of OA⁷²), cartilage lesions and damaged nociceptors lead to neuropathic pain. In this study, we hypothesize that prophylactic administration of RvD1 prevents the initial surge in inflammatory factors, thus effectively inhibiting tissue damage. On the contrary, as the therapeutic administration is done later, it is possible that excessive early inflammation causes nerve damage and subsequent neuropathic pain to prevail.

Our administration frequencies were inspired by Sun et al., with certain changes.²⁸ The first (of the two injections) administration for prophylactic treatment was performed 5-6 days after the surgery as such a prophylactic dose is feasible for human use in case of severe trauma to the joints. Similarly, the first dose for the therapeutic regimen was administered 3 weeks after surgery because, by this time, the pathology in the joint is reported to progress significantly.^{30,46}

Recent reports show that body composition, not body weight, has a true bearing on joint health.⁷³⁻⁷⁵ Although we show that an increase in body weight by sustained high-fat feeding increases serum lipids (an indicator of high body fat), this remains indirect evidence of a body composition comprised of high fat. In future experiments, direct quantification of body composition can be performed using powerful techniques like DEXA scanning.⁷⁶

A limitation of this study is that the experiments in this study utilized only male mice as surgery-induced-OA shows more dramatic

effects on the cartilage of male mice than that of female mice.³¹ ObOA can be reproducibly mimicked in HFD-fed obese mice by performing DMM surgery on the respective stifle joints. This model also shows certain similarities with the etiology of disease in humans.⁷⁷ However, it is not possible to mimic the load-bearing patterns in the articulating joints of large bipeds (humans) in small quadrupeds like mice.^{78,79} Similarly, the vast difference in the sizes of the joints results in unpredictable and unscalable pharmacokinetics of the molecule, which accounts for poor translation to clinics. Hence for future translation, further testing is required in larger animals. Another limitation of this study is the inability to detect osteophytes using the techniques described earlier. This detection can be performed in future studies using more sensitive techniques like microCT.

5 | CONCLUSION

In this study, we formulated nanoliposomes that arrested cartilage damage in an ObOA model of mice. The controlled release of RvD1 was achieved for ~11 days. Lipo-RvD1 promoted the M2 polarization of macrophages in the synovium which mediated resolution of inflammation resulting in substantially less cartilage damage. This formulation also reduced disease symptoms like OA-associated pain when used as a prophylactic regimen. Lipo-RvD1 has shown encouraging efficacy as both a prophylactic and therapeutic agent and can thus be a promising strategy to treat OA.

ACKNOWLEDGMENTS

We thank Prof Sathees Raghavan and Prof Sanhita Sinharay for access to the instruments used in this study. We also thank Central Animal Facility (CAF) for breeding and maintaining mice. Dr Dhanusha G. and Dr Thirumala M.'s help with scoring histological sections is also acknowledged. Finally, we would like to acknowledge Early Career Research Award (Science and Engineering Research Board, Department of Science and Technology, India, ECR/2017/002178), Har Gobind Khorana Innovative Young Biotechnologist Award (Department of Biotechnology, BT/12/IYBA/2019/04), Indian Institute of Science start-up grant, Private funding from Mr Lakshmi Narayan, and Private funding from Dr Vijaya and Rajagopal Rao funding for Biomedical Engineering research at the Centre for BioSystems Science and Engineering and express our gratitude for funding this research.

CONFLICT OF INTEREST STATEMENT

The authors declare no conflict of interest.

DATA AVAILABILITY STATEMENT

The data that support the findings of this study are available from the corresponding author upon reasonable request.

REFERENCES

- Long H, Liu Q, Yin H, et al. Prevalence trends of site-specific osteoarthritis from 1990 to 2019: findings from the global burden of disease study 2019. *Arthritis Rheum.* 2022;74:1172-1183.
- Messier SP. Obesity and osteoarthritis: disease genesis and nonpharmacologic weight management. *Rheum Dis Clin North America.* 2008;34:713-729.
- King L, March L, Anandacoomarasamy A. Obesity & osteoarthritis. *Indian J Med Res.* 2013;138:185-193.
- Jones IA, Togashi R, Wilson ML, Heckmann N, Jr CTV. Intra-articular treatment options for knee osteoarthritis. *Nat Rev Rheumatol.* 2019;15:77-90.
- Jayaram P, Kennedy D, Yeh P, Dragoo J. Chondrotoxic effects of local anesthetics on human knee articular cartilage: a systematic review. *Am Acad Phys Med Rehabil.* 2019;11:379-400.
- Ellulu MS, Patimah I, Khaza'ai H, Rahmat A, Abed Y. Obesity and inflammation: the linking mechanism and the complications. *Arch Med Sci.* 2015;13:851-863.
- Griffin T, Huebner J, Kraus V, Guilak F. Extreme obesity due to impaired leptin signaling in mice does not cause knee osteoarthritis. *Arthritis Rheum.* 2009;60:2935-2944.
- Wang T, He C. Pro-inflammatory cytokines: the link between obesity and osteoarthritis. *Cytokine Growth Factor Rev.* 2018;44:38-50.
- Chevalier X, Ravaud P, Maheu E, et al. Adalimumab in patients with hand osteoarthritis refractory to analgesics and NSAIDs: a randomised, multicentre, double-blind, placebo-controlled trial. *Ann Rheum Dis.* 2015;74:1697-1705.
- Chevalier X, Giraudeau B, Conrozier T, Marliere J, Kiefer P, Goupille P. Safety study of intraarticular injection of interleukin 1 receptor antagonist in patients with painful knee osteoarthritis: a multicenter study. *J Rheumatol.* 2005;32:1317-1323.
- Chisari E, Yaghtmour KM, Khan WS. The effects of TNF-alpha inhibition on cartilage: a systematic review of preclinical studies. *Osteoarthritis Cartil.* 2020;28:708-718.
- Vincent TL. IL-1 in osteoarthritis: time for a critical review of the literature. *F1000 Res.* 2019;8. <https://f1000research.com/articles/8-934/v1>
- Evans C, Kraus V, Setton L. Progress in intra-articular therapy. *Nat Rev Rheumatol.* 2014;10:11-22.
- Simkin PA. Synovial perfusion and synovial fluid solutes. *Ann Rheum Dis.* 1995;54:424-428.
- Larsen C, Østergaard J, Larsen SW, et al. Intra-articular depot formulation principles: role in the management of postoperative pain and arthritic disorders. *J Pharm Sci.* 2008;97:4622-4653.
- Dravid A, Dhanabalan K, Agarwal S, Agarwal R. Resolvin D1-loaded nanoliposomes promote M2 macrophage polarization and are effective in the treatment of osteoarthritis. *Bioeng Transl Med.* 2022;7:e10281.
- Lyu Y, Xiao Q, Yin L, Yang L, He W. Potent delivery of an MMP inhibitor to the tumor microenvironment with thermosensitive liposomes for the suppression of metastasis and angiogenesis. *Signal Transduct Target Ther.* 2019;4:1-9.
- Ozbakir B, Crielaard B, Metselaar J, Storm G, Lammers T. Liposomal corticosteroids for the treatment of inflammatory disorders and cancer. *J Control Release.* 2014;190:624-636.
- Xia Y, Xu C, Zhang X, et al. Liposome-based probes for molecular imaging: from basic research to the bedside. *Nanoscale.* 2019;11:5822-5838.
- Elron-Gross I, Glucksam Y, Margalit R. Liposomal dexamethasone-diclofenac combinations for local osteoarthritis treatment. *Int J Pharm.* 2009;376:84-91.
- Dong J, Jiang D, Wang Z, Wu G, Miao L, Huang L. Intra-articular delivery of liposomal celecoxib-hyaluronate combination for the treatment of osteoarthritis in rabbit model. *Int J Pharm.* 2013;441:285-290.
- Sohn HS, Choi JW, Jhun JY, et al. Tolerogenic nanoparticles induce type II collagen-specific regulatory T cells and ameliorate osteoarthritis. *Sci Adv.* 2022;8:eabo5284.
- Buckley C, Gilroy D, Serhan C. Pro-resolving lipid mediators and mechanisms in the resolution of acute inflammation. *Immunity.* 2014;40:1-26.

24. Headland S, Norling L. The resolution of inflammation: principles and challenges. *Semin Immunol*. 2015;27:149-160.
25. Fullerton J, Gilroy D. Resolution of inflammation: a new therapeutic frontier. *Nat Rev Drug Discov*. 2016;15:551-567.
26. Reina-Couto M, Carvalho J, Valente MJ, et al. Impaired resolution of inflammation in human chronic heart failure. *Eur J Clin Invest*. 2014;44:527-538.
27. Merched A, Ko K, Gotlinger K, Serhan C, Chan L. Atherosclerosis: evidence for impairment of resolution of vascular inflammation governed by specific lipid mediators. *FASEB J*. 2008;22:3595-3606.
28. Sun AR, Wu X, Liu B, et al. Pro-resolving lipid mediator ameliorates obesity induced osteoarthritis by regulating synovial macrophage polarisation. *Sci Rep*. 2019;9:1-13.
29. Huang H, Skelly J, Ayers D, Song J. Age-dependent changes in the articular cartilage and subchondral bone of C57BL/6 mice after surgical destabilization of medial meniscus. *Sci Rep*. 2017;7:1-9.
30. Glasson SS, Blanchet TJ, Morris EA. The surgical destabilization of the medial meniscus (DMM) model of osteoarthritis in the 129/SvEv mouse. *Osteoarthr Cartil*. 2007;15:1061-1069.
31. Ma HL, Blanchet TJ, Peluso D, Hopkins B, Morris EA, Glasson SS. Osteoarthritis severity is sex dependent in a surgical mouse model. *Osteoarthr Cartil*. 2007;2007:695-700.
32. Pastoureau P, Chomel A. Methods for cartilage and subchondral bone histomorphometry. *Method in Molecular Medicine*. Vol 101. Springer; 2004:79-91.
33. Pritzker KPH, Gay S, Jimenez SA, et al. Osteoarthritis cartilage histopathology: grading and staging. *Osteoarthr Cartil*. 2006;14:13-29.
34. Dhanabalan KM, Dravid A, Agarwal S, Sharath R, Padmanabhan A, Agarwal R. Intra-articular injection of rapamycin microparticles prevent senescence and effectively treat osteoarthritis. *Bioeng Transl Med*. 2022;8:e10298.
35. Kopelman PG. Obesity as a medical problem. *Nature*. 2000;404:635-643.
36. Devlin MJ, Robbins A, Cosman MN, et al. Differential effects of high fat diet and diet-induced obesity on skeletal acquisition in female C57BL/6J vs FVB/NJ mice. *Bone Rep*. 2018;8:204-214.
37. Lin S, Thomas TC, Storlien LH, Huang XF. Development of high fat diet-induced obesity and leptin resistance in C57BL/6J mice. *Int J Obes (Lond)*. 2000;24:639-646.
38. Klop B, Elte JW, Cabezas MC. Dyslipidemia in obesity: mechanisms and potential targets. *Nutrients*. 2013;5:1218-1240.
39. Nikolic D, Katsiki N, Montalto G, Isenovic E, Mikhailidis D, Rizzo M. Lipoprotein subfractions in metabolic syndrome and obesity: clinical significance and therapeutic approaches. *Nutrients*. 2013;5:928-948.
40. Eisinger K, Liebisch G, Schmitz G, Aslanidis C, Krautbauer S, Buechler C. Lipidomic analysis of serum from high fat diet induced obese mice. *Int J Mol Sci*. 2014;15:2991-3002.
41. Sica A, Erreni M, Allavena P, Porta C. Macrophage polarization in pathology. *Cell Mol Life Sci*. 2015;72:4111-4126.
42. Shapouri-Moghaddam A, Mohammadian S, Vazini H, et al. Macrophage plasticity, polarization, and function in health and disease. *J Cell Physiol*. 2018;233:6425-6440.
43. Liu B, Zhang M, Zhao J, Zheng M, Yang H. Imbalance of M1/M2 macrophages is linked to severity level of knee osteoarthritis. *Exp Ther Med*. 2018;16:5009-5014.
44. Carlson EL, Karuppagounder V, Pinamont WJ, et al. Paroxetine-mediated GRK2 inhibition is a disease-modifying treatment for osteoarthritis. *Sci Transl Med*. 2021;13:1-14.
45. Braun HJ, Gold GE. Diagnosis of osteoarthritis: imaging. *Bone*. 2012;51:278-288.
46. Fang H, Huang L, Welch I, et al. Early changes of articular cartilage and subchondral bone in the DMM mouse model of osteoarthritis. *Sci Rep*. 2018;8:1-9.
47. Luyten F, Tylzanowski P, Lories R. Wnt signaling and osteoarthritis. *Bone*. 2009;44:522-527.
48. Yazici Y, McAlindon TE, Gibofsky A, et al. A Phase 2b randomized trial of lorecivivint, a novel intra-articular CLK2/DYRK1A inhibitor and Wnt pathway modulator for knee osteoarthritis. *Osteoarthr Cartil*. 2021;29:654-666.
49. Wenham C, Conaghan P. The role of synovitis in osteoarthritis. *Ther Adv Musculoskelet Dis*. 2010;2:349-369.
50. Lange-Brokaar BJE, Ioan-Facsinay A, van Osch GJ, et al. Synovial inflammation, immune cells and their cytokines in osteoarthritis: a review. *Osteoarthr Cartil*. 2012;20:1484-1499.
51. Conaghan P, Cook A, Hamilton J, Tak P. Therapeutic options for targeting inflammatory osteoarthritis pain. *Nat Rev Rheumatol*. 2019;15:355-363.
52. Pottier P, Presle N, Terlain B, Netter P, Mainard D, Berenbaum F. Obesity and osteoarthritis: more complex than predicted! *Ann Rheum Dis*. 2006;65:1403-1405.
53. Simopoulos A. An increase in the omega-6/omega-3 fatty acid ratio increases the risk for obesity. *Nutrients*. 2016;8:1-17.
54. Clària J, Dalli J, Yacoubian S, Gao F, Serhan CN. Resolvin D1 and Resolvin D2 govern local inflammatory tone in obese fat. *J Immunol*. 2012;189:2597-2605.
55. Liu H-Q, Qiu Y, Mu Y, et al. A high ratio of dietary n-3/n-6 polyunsaturated fatty acids improves obesity-linked inflammation and insulin resistance through suppressing activation of TLR4 in SD rats. *Nutr Res*. 2013;33:849-858.
56. Schunck W-H, Konkel A, Fischer R, Weylandt K-H. Therapeutic potential of omega-3 fatty acid-derived epoxyeicosanoids in cardiovascular and inflammatory diseases. *Pharmacol Ther*. 2018;183:177-204.
57. Wu C-L, Jain D, McNeill JN, et al. Dietary fatty acid content regulates wound repair and the pathogenesis of osteoarthritis following joint injury. *Ann Rheum Dis*. 2015;74:2076-2083.
58. Knott L, Avery NC, Hollander AP, Tarlton JF. Regulation of osteoarthritis by omega-3 (n-3) polyunsaturated fatty acids in a naturally occurring model of disease. *Osteoarthr Cartil*. 2011;19:1150-1157.
59. Gemperle C, Tran S, Schmid M, et al. Resolvin D1 reduces inflammation in co-cultures of primary human macrophages and adipocytes by triggering macrophages. *Prostaglandins Leukot Essent Fatty Acids*. 2021;174:102363.
60. Atri C, Guerfali F, Laouini D. Role of human macrophage polarization in inflammation during infectious diseases. *Int J Mol Sci*. 2018;19:2-15.
61. Lisi L, Ciotti GMP, Braun D, et al. Expression of iNOS, CD163 and ARG-1 taken as M1 and M2 markers of microglial polarization in human glioblastoma and the surrounding normal parenchyma. *Neurosci Lett*. 2017;3:106-112.
62. Jensen TS, Finnerup NB. Allodynia and hyperalgesia in neuropathic pain: clinical manifestations and mechanisms. *Lancet Neurol*. 2014;13:924-935.
63. Zheng J. Molecular mechanism of TRP channels. *Compr Physiol*. 2013;3:1-43.
64. Hinata M, Imai S, Sanaki T, et al. Sensitization of transient receptor potential vanilloid 4 and increasing its endogenous ligand 5,6-epoxyeicosatrienoic acid in rats with monoiodoacetate-induced osteoarthritis. *Pain*. 2018;159:939-947.
65. Kelly S, Chapman RJ, Woodhams S, et al. Increased function of nociceptive TRPV1 at the level of the joint in a rat model of osteoarthritis pain. *Ann Rheum Dis*. 2015;74:252-259.
66. Valdes A, de Wilde G, Doherty SA, et al. The Ile585Val TRPV1 variant is involved in risk of painful knee osteoarthritis. *Ann Rheum Dis*. 2011;70:1556-1561.
67. Roh J, Go EJ, Park J-W, Kim YH, Park C-K. Resolvins: potent pain inhibiting lipid mediators via transient receptor potential regulation. *Front Cell Dev Biol*. 2020;8:1-15.
68. Bang S, Yoo S, Yang TJ, Cho H, Kim YG, Hwang SW. Resolvin D1 attenuates activation of sensory transient receptor potential channels leading to multiple anti-nociception. *Br J Pharmacol*. 2010;161:707-720.

69. Huang J, Burston JJ, Li L, et al. Targeting the D series resolvins receptor system for the treatment of osteoarthritis pain. *Arthritis Rheumatol*. 2017;69:996-1008.
70. Lee W, Nims RJ, Savadipour A, et al. Inflammatory signaling sensitizes Piezo1 mechanotransduction in articular chondrocytes as a pathogenic feed-forward mechanism in osteoarthritis. *Proc Natl Acad Sci USA*. 2021;118:e2001611118. <https://www.pnas.org/doi/full/10.1073/pnas.2001611118>
71. Eitner A, Pester J, Nietzsche S, Hofmannz GO, Schaible HG. The innervation of synovium of human osteoarthritic joints in comparison with normal rat and sheep synovium. *Osteoarthr Cartil*. 2013;21:1383-1391.
72. Kohei Murakami HN, Nishimura K, Matsuo S. Changes in peptidergic fiber density in the synovium of mice with collagenase-induced acute arthritis. *Can J Physiol Pharmacol*. 2015;93:431-441.
73. Long H, Xie D, Zeng C, et al. Association between body composition and osteoarthritis: a systematic review and meta-analysis. *Int J Rheum Dis*. 2019;22:2108-2118.
74. Wen L, Kang JH, Yim YR, et al. Associations between body composition measurements of obesity and radiographic osteoarthritis in older adults: data from the Dong-gu study. *BMC Musculoskelet Disord*. 2016;17:192.
75. Nur H, Tuncer T. The relationship between body composition and knee osteoarthritis in postmenopausal women. *Turk J Phys Med Rehabil*. 2018;64:121-125.
76. Erselcan T, Candan F, Saruhan S, Ayca T. Comparison of body composition analysis methods in clinical routine. *Ann Nutr Metab*. 2000;44:243-248.
77. Chen D, Shen J, Zhao W, et al. Osteoarthritis: toward a comprehensive understanding of pathological mechanism. *Bone Res*. 2017;5:1-13.
78. Teeple E, Jay G, Elsaid K, Fleming B. Animal models of osteoarthritis: challenges of model selection and analysis. *AAPS J*. 2013;15:438-456.
79. Cook JL, Hung CT, Kuroki K, et al. Animal models of cartilage repair. *Bone Joint Res*. 2014;3:89-94.

SUPPORTING INFORMATION

Additional supporting information can be found online in the Supporting Information section at the end of this article.

How to cite this article: Dravid AA, Dhanabalan KM, Naskar S, et al. Sustained release resolvins D1 liposomes are effective in the treatment of osteoarthritis in obese mice. *J Biomed Mater Res*. 2023;111(6):765-777. doi:[10.1002/jbm.a.37512](https://doi.org/10.1002/jbm.a.37512)